

# Phase separation of YAP reorganizes genome topology for long-term YAP target gene expression

Danfeng Cai<sup>1,2</sup>, Daniel Feliciano<sup>2,3</sup>, Peng Dong<sup>2</sup>, Eduardo Flores<sup>4</sup>, Martin Gruebele<sup>5</sup>, Natalie Porat-Shliom<sup>3</sup>, Shahar Sukenik<sup>4,5</sup>, Zhe Liu<sup>2</sup> and Jennifer Lippincott-Schwartz<sup>1,2\*</sup>

**Yes-associated protein (YAP) is a transcriptional co-activator that regulates cell proliferation and survival by binding to a select set of enhancers for target gene activation. How YAP coordinates these transcriptional responses is unknown. Here, we demonstrate that YAP forms liquid-like condensates in the nucleus. Formed within seconds of hyperosmotic stress, YAP condensates compartmentalized the YAP transcription factor TEAD1 and other YAP-related co-activators, including TAZ, and subsequently induced the transcription of YAP-specific proliferation genes. Super-resolution imaging using assay for transposase-accessible chromatin with photoactivated localization microscopy revealed that the YAP nuclear condensates were areas enriched in accessible chromatin domains organized as super-enhancers. Initially devoid of RNA polymerase II, the accessible chromatin domains later acquired RNA polymerase II, transcribing RNA. The removal of the intrinsically-disordered YAP transcription activation domain prevented the formation of YAP condensates and diminished downstream YAP signalling. Thus, dynamic changes in genome organization and gene activation during YAP reprogramming is mediated by liquid-liquid phase separation.**

The nuclear localization of the transcriptional co-activator yes-associated protein (YAP) and activation of the TEA domain family (TEAD) transcription factors promote cell proliferation, differentiation and stem-cell fate<sup>1–3</sup>, with deficiencies in YAP regulation leading to developmental defects and cancer progression<sup>1</sup>. The nuclear localization of YAP is regulated by the Hippo pathway, an evolutionarily conserved signalling system that responds to mechano-chemically induced changes in tissue architecture and osmolarity<sup>4–6</sup>. Despite the importance of YAP, little is known regarding the precise mechanisms that lead to alteration of gene expression patterns when YAP is redistributed into the nucleus.

Phase separation of proteins and nucleic acids into liquid-like or gel-like condensates (also called ‘droplets’) in cells arises through a process involving weak multivalent interactions among these molecules<sup>7–9</sup>. In the nucleus, such phase separation has recently been shown to contribute to heterochromatin formation<sup>10,11</sup>, transcriptional upregulation<sup>12–14</sup> and the clustering of nuclear enhancer elements and bound transcription-related factors into sites called super-enhancers<sup>15</sup>, which transcribe discrete sets of genes important for cell identity or cancer malignancy<sup>15,16</sup>.

YAP has been shown to interact with various transcription elongation factors and can act at super-enhancer regions in the genome<sup>17,18</sup>. Given this and the above-mentioned suggestion of the involvement of liquid–liquid phase separation in the formation of super-enhancers, we investigated whether YAP forms phase condensates to activate its gene expression program. As previous work has shown that hyperosmotic stress activates YAP downstream signalling, we examined the localization of YAP following hyperosmotic stress. We found that YAP formed nuclear- and cytoplasmic-phase condensates immediately following hyperosmotic stress.

The condensates contained different sets of proteins, which contributed to both the ability of YAP to redistribute into the nucleus and its role in transcriptional control. In the nucleus, YAP droplets were shown to reorganize the genome for driving long-term expression of YAP target genes.

## Results

**YAP has an intrinsic ability to phase separate into condensates.** Analysis of the YAP amino acid sequence using algorithms that predict the disordered regions in proteins revealed YAP has an extended C-terminal low-complexity region encompassing a transcription activation domain (TAD; Fig. 1a), which is known to mediate phase separation in other transcription cofactors<sup>13</sup>. The non-ionic crowder polyethylene glycol (PEG) was added to purified enhanced green fluorescent protein (EGFP)-YAP from *Escherichia coli* to assess whether YAP can form liquid condensates in vitro. This produced a turbid EGFP-YAP solution, in contrast to that found for purified EGFP (Fig. 1b,c). Confocal imaging of EGFP-YAP revealed the formation of micrometre-sized spheres under crowding conditions (Fig. 1d). The spheres displayed characteristics of liquid-like condensates<sup>19</sup>, including droplet coalescence (Fig. 1e), wetting the coverslip (Supplementary Video 1) and the ability to disperse following resuspension in buffer with no crowder (Fig. 1d, washed). The reversibility of the EGFP-YAP droplets showed they were not aggregated particles incapable of rapidly disassembling. Other conditions known to affect phase separation of proteins (that is, salts, inert proteins and nucleic acids)<sup>19,20</sup> did not trigger the formation of YAP droplets (Extended Data Fig. 1a). The intrinsically-disordered YAP TAD domain was required for YAP phase separation, as YAP that lacked this domain (that is, EGFP-YAPΔTAD) failed to

<sup>1</sup>Eunice Kennedy Shriver National Institute for Child Health and Human Development, National Institutes of Health, Bethesda, MD, USA. <sup>2</sup>Janelia Research Campus, Howard Hughes Medical Institute, Ashburn, VA, USA. <sup>3</sup>Thoracic and Malignancies Branch, National Cancer Institute, National Institutes of Health, Bethesda, MD, USA. <sup>4</sup>Department of Chemistry and Chemical Biology, University of California, Merced, CA, USA. <sup>5</sup>Department of Chemistry, University of Illinois at Urbana-Champaign, Urbana, IL, USA. \*e-mail: lippincottschwartz@janelia.hhmi.org

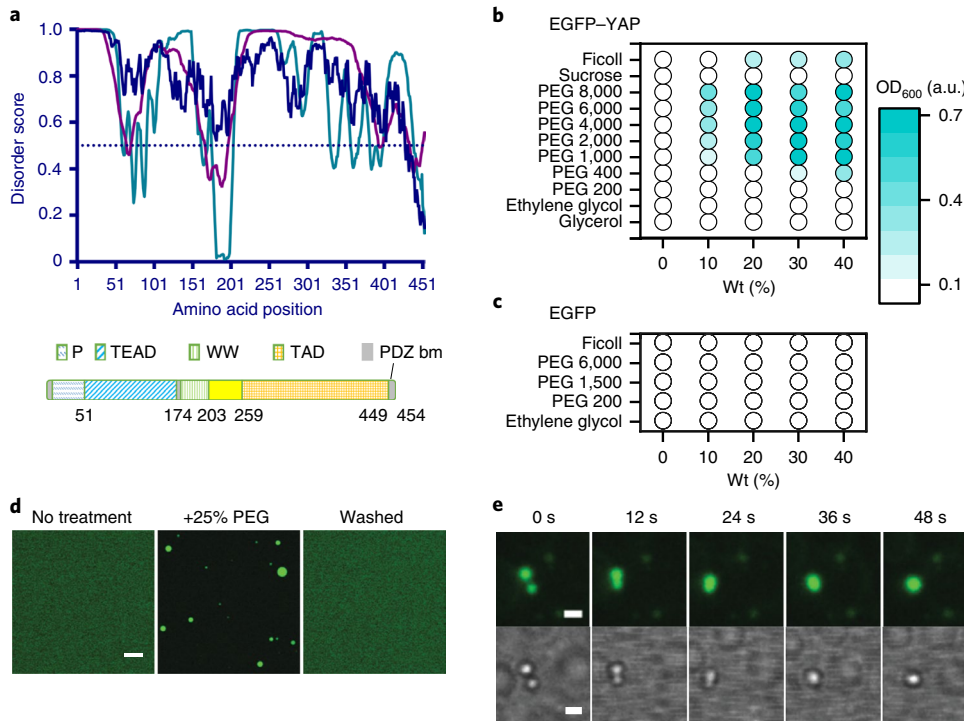


**Fig. 1 | YAP has an intrinsic ability to phase separate.** **a**, Disorder analysis of the YAP 454 amino acid isoform (top). The algorithms used were: IUPred (blue), VLXT (cyan) and VSL2 (magenta). Dotted line indicates 0.5 disordered score, above which the amino acid sequence is disordered. Diagram below shows the domains and boundaries of the domains of YAP protein. **b,c**, Purified EGFP-YAP shows a concentration-dependent increase in turbidity at increasing levels of large polymeric crowders (**b**), whereas purified EGFP does not (**c**). The legend in **b** also applies to **c**. **d**, EGFP-YAP before (left) and after (middle) the addition of 25% PEG. The droplets disappear following centrifugation and resuspension in isotonic buffer (right). The experiment was repeated three times independently with similar results. **e**, Droplet coalescence shown under fluorescent (top) and bright-field (bottom) illumination. The experiment was repeated three times independently with similar results. Scale bars, 10 μm (**d**) and 2 μm (**e**).

undergo phase separation under crowding concentrations similar to that seen for EGFP-YAP (Extended Data Fig. 1b).

**YAP undergoes phase separation into cytoplasmic and nuclear condensates in hyperosmotically stressed cells.** YAP is known to redistribute into the nucleus to drive the transcription of proliferation-specific genes under conditions such as hyperosmotic stress<sup>6</sup>. We found that the transcription of the YAP target genes *Ctgf* and *Cyr61* in HEK293T cells increased by sixfold and threefold, respectively, within 3 h following the addition of the hyperosmotic reagent d-sorbitol (0.2 M; Fig. 2a). Similar results were observed in response to the addition of PEG 300 (Fig. 2b).

When examining how hyperosmotic stress impacts the subcellular distribution of YAP, we observed that EGFP-YAP shifted from being uniformly dispersed in the cytoplasm to being concentrated in discrete puncta in the cytoplasm and nucleus (Fig. 2c, top panel). The puncta formed within 20 s of sorbitol treatment and seemed to be spherical in zoomed-in images (Fig. 2d). EGFP expressed in these cells showed no change in subcellular distribution following hyperosmotic stress (Fig. 2c, lower panel). The EGFP-YAP puncta persisted for 1 h and then decreased in number until only a few nuclear condensates were left after 3 h in sorbitol (Fig. 2c, upper panel and Fig. 2e). Washing with isotonic medium when the puncta were still present caused the puncta to completely disappear within 5 min (Fig. 2f,g).

The EGFP-YAP puncta in hyperosmotically stressed cells exhibited key features of phase-separated condensates<sup>7,21</sup>, including high sphericity (Extended Data Fig. 2a), fusion behaviour (Fig. 2h and Supplementary Videos 2–4) and rapid fluorescence recovery following photobleaching (half-time ( $t_{1/2}$ ) = 0.9 ± 0.4 s; Fig. 2i,j).

The formation of these puncta was independent of the YAP isoform (Extended Data Fig. 2b), not limited to the specific osmotic agent used (Extended Data Fig. 2c) and occurred in many cell types (Extended Data Fig. 2d), all of which underwent volume reduction (Extended Data Fig. 2e) and showed increased macromolecular crowding (Extended Data Fig. 2f,g) in response to the hyperosmotic stress.

**Endogenous YAP in cells forms condensates.** Using a YAP-specific antibody to label endogenous YAP in HEK293 cells, we found that small puncta became visible in the nucleus within 10 min of sorbitol treatment (Fig. 3a). Similar to EGFP-YAP, the antibody-labelled condensates dissipated after 3 h of sorbitol treatment. Knockdown of YAP by RNA interference (RNAi) reduced the expression of YAP protein—measured by immunoblotting and immunofluorescence (Extended Data Fig. 3a,b)—and eliminated the YAP foci observed in response to sorbitol treatment (Fig. 3b).

We also generated a clustered regularly interspaced short palindromic repeats (CRISPR) knock-in U-2 OS cell line, in which a HaloTag was fused to the C terminus of the YAP genomic loci to generate cells with the endogenous YAP replaced with YAP-HaloTag (Extended Data Fig. 3c). YAP-HaloTag nuclear puncta appeared within 10 min of hyperosmotic stress induced by either 0.2 M sorbitol (Fig. 3c,d) or 10% PEG 300 (Extended Data Fig. 3d,e). The puncta recovered rapidly after photobleaching (Fig. 3e) and could be decorated with anti-YAP antibodies (Fig. 3f). The knock-down of YAP with RNAi to remove YAP-HaloTag/YAP in these cells resulted in no anti-YAP-labelled condensates (Fig. 3g,h).

We next examined the localization of YAP in the cells of the mouse kidney, a tissue known to experience hyperosmotic stress,

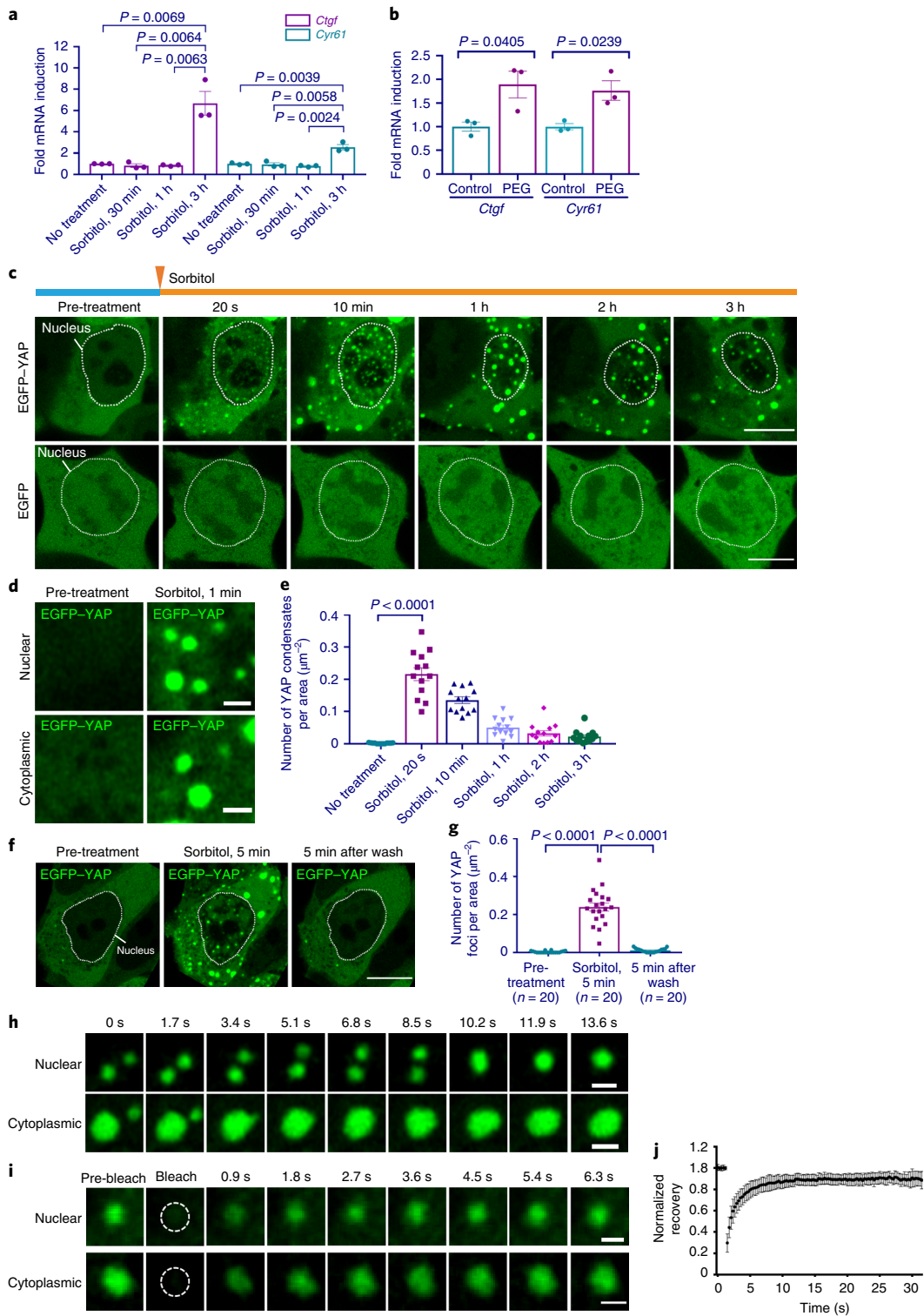


**Fig. 2 | YAP undergoes phase separation under hyperosmotic stress.** **a**, Relative mRNA levels of *Ctgf* and *Cyr61* in control and sorbitol-treated HEK293T cells expressing EGFP-YAP. Two-sided unpaired t-test;  $n=3$  biologically independent samples. **b**, Relative levels of *Ctgf* and *Cyr61* mRNA in HEK293T cells expressing EGFP-YAP 3 h after treatment with or without 5% PEG 300. Two-sided unpaired t-test;  $n=3$  biologically independent samples. **c**, EGFP-YAP (top), but not EGFP (bottom), localizes to the nucleus of HEK293T cells and forms cytoplasmic and nuclear foci 20 s after sorbitol treatment. **d**, Zoomed-in live-cell images of the nuclear and cytoplasmic YAP condensates formed before and after 1 min in sorbitol. **e**, Number of EGFP-YAP foci in HEK293T cells normalized to the cell area at the indicated times following sorbitol treatment. Two-sided paired t-test;  $n=13$  biologically independent samples. **f**, Live-cell images showing that the formation of EGFP-YAP condensates is reversible. **g**, Quantification of the formation of reversible EGFP-YAP condensates. Two-sided paired t-test. **h**, Time-lapse imaging of the fusion of nuclear and cytoplasmic EGFP-YAP droplets. The experiment was repeated at least five times independently with similar results. **i**, FRAP recovery images of nuclear and cytoplasmic EGFP-YAP condensates. The dotted circle indicates the region of photobleaching. **j**, FRAP recovery curve of EGFP-YAP condensates averaged from  $n=26$  biologically independent experiments. The centres of the data indicate the mean and the error bars show the s.e.m. (**a,b,e,g,j**) or s.d. (**j**). Scale bars, 10  $\mu\text{m}$  (**c,f**) and 1  $\mu\text{m}$  (**d,h,i**). Statistics source data are provided in Source Data Fig. 2.

with kidney medulla cells experiencing a more hyperosmotic environment than cortical cells<sup>22–25</sup> (Fig. 3*i*). The localization of the YAP antibody in cortical kidney cells was restricted primarily to the cytoplasm (Fig. 3*j*, top and Fig. 3*k*), with few (if any) nuclear puncta seen (Fig. 3*j*, top and Fig. 3*l*). In contrast, YAP in medulla cells was enriched in the nucleus (Fig. 3*j*, bottom and Fig. 3*k*) and contained prominent punctate structures that resembled the YAP nuclear condensates observed in osmotically stressed HEK293T and U-2 OS cells (Fig. 3*j*, bottom and Fig. 3*l*).

**Characterization of cytoplasmic YAP condensates induced by hyperosmotic stress.** We found that the YAP cytoplasmic condensates concentrated proteins involved in YAP-specific post-translational modifications, including the Hippo-pathway kinase large tumour suppressor 1 (LATS1; Fig. 4*a*) and nemo-like kinase (NLK; Fig. 4*b*). Given that previous work has shown that hyperosmotic stress leads to the activation of both NLK and LATS1/2 (ref. <sup>6</sup>), these findings raised the possibility that the localization of NLK and LATS1/2 in cytoplasmic YAP condensates might coordinate the activity of both kinases.

LATS1/2 is known to phosphorylate YAP at Ser127, causing it to become more tightly associated with 14-3-3 proteins and to be retained in the cytoplasm<sup>26,27</sup>. Because there was less mCherry-YAP localized in the nucleus of cells overexpressing EGFP-LATS1 compared with cells not expressing EGFP-LATS1 after sorbitol treatment (compare Figs. 4*a* and 2*c*), the data suggested that the enhanced phosphorylation of YAP at Ser127 helps retain YAP in the cytoplasm in EGFP-LATS1-overexpressing cells. Consistent with this, the mutation of the serine at position 127 in YAP to alanine (to prevent phosphorylation by LATS) significantly increased the nuclear localization of YAP during hyperosmotic shock (Fig. 4*d*).

NLK phosphorylates YAP at Ser128, releasing the YAP bound to 14-3-3 proteins to allow YAP nuclear import<sup>28</sup>. We mutated YAP Ser128 to an alanine to test whether phosphorylation of YAP at Ser128 in cytoplasmic droplets helps promote the nuclear redistribution of YAP in NLK-expressing cells. We found that this significantly impaired the ability of YAP to become localized to the nucleus in response to hyperosmotic shock (Fig. 4*d*), without impairing its ability to form droplets (Fig. 4*c*).

The YAP cytoplasmic droplets did not contain the stress-granule component G3BP (Fig. 4*e*) or co-segregate with G3BP-containing stress granules during arsenite treatment (Fig. 4*f*). They also were not processing bodies (P-bodies) involved in RNA processing, as they lacked critical P-body components, including GW182 and Ago2 (Extended Data Fig. 4*a–d*). However, the P-body component Dcp1a did co-segregate with YAP droplets (Fig. 4*g*), suggesting some unknown link to RNA processing. Altogether, the data

revealed that the YAP cytoplasmic condensates are neither stress granules nor P-bodies but are a type of cytoplasmic droplet that sequesters kinases, which target YAP for either cytoplasmic retention or nuclear translocation.

**Characterization of nuclear YAP condensates induced by hyperosmotic stress.** The YAP nuclear condensates did not colocalize with known nuclear body markers, such as PML (promyelocytic leukaemia bodies; Fig. 5*a,b*) or coilin (Cajal bodies; Fig. 5*c,d*), suggesting they perform functions different from these well-known nuclear bodies. Instead, the YAP condensates were enriched in the transcription factor TEAD1 (Fig. 5*e,f*), which regulates the transcription of YAP target genes<sup>1,29,30</sup>. Neither YAP nor TEAD1 were found in nuclear or cytoplasmic droplets before sorbitol treatment. However, both molecules were found colocalized in nuclear condensates within 2 min of hypertonic stress. Line scans through the condensates showed a similar profile of enrichment for each protein in the droplet (Fig. 5*f*). A similar colocalization of YAP and TEAD1 in droplets was observed in U-2 OS cells in response to hyperosmotic stress induced by PEG (Extended Data Fig. 5*a,b*).

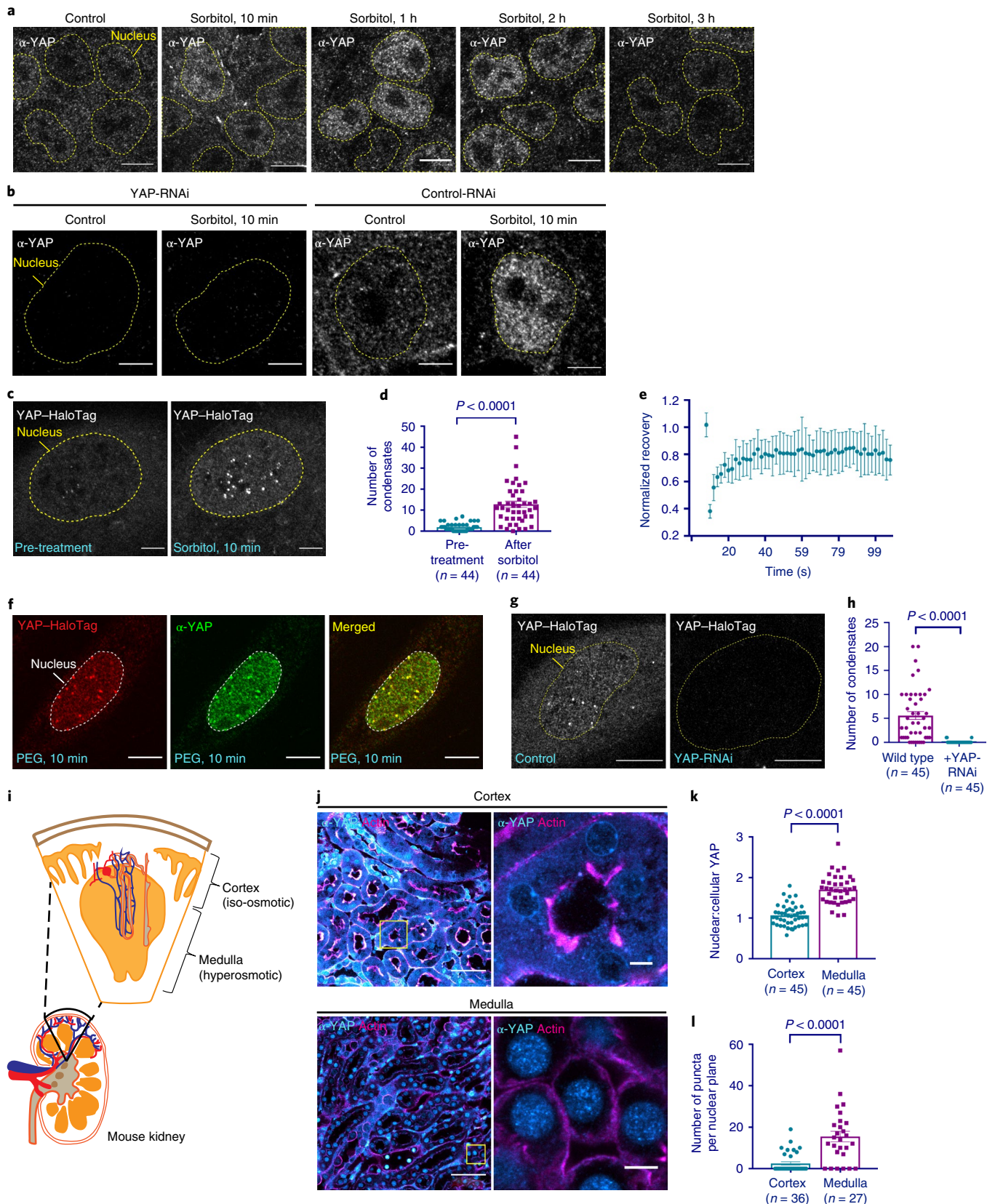
The YAP nuclear condensates also contained the YAP paralog WW-domain-containing transcription regulator (TAZ; Fig. 5*g,h*), which was recently reported in nuclear phase condensates<sup>31</sup>. Both TAZ and YAP were homogenously dispersed in the cytoplasm of HEK293T cells before hyperosmotic treatment but redistributed into nuclear droplets within 20 s of treatment (Fig. 5*g*). YAP and TAZ showed a similar overall distribution in the droplets (Fig. 5*h*). Coexpression of EGFP-TAZ and mCherry-YAP in U-2 OS cells revealed the two molecules colocalized in the same droplets after hyperosmotic stress (Extended Data Fig. 5*c*). Observation of the same cell before and after hyperosmotic treatment revealed mCherry-YAP redistributed into pre-existing EGFP-TAZ droplets, as well as into new droplets, into which EGFP-TAZ later redistributed (Extended Data Fig. 5*c*).

**3D ATAC-PALM reveals YAP nuclear condensates localize to spatially segregated accessible chromatin domains.** The linear distribution of chromatin accessible for binding by transcription factors, promoters and insulators has been mapped through DNase I digestion<sup>32,33</sup> and using an assay for transposase-accessible chromatin (ATAC) with high-throughput sequencing (ATAC-seq)<sup>34</sup>, revealing that many gene-enhancer elements cluster with their transcription factors into super-enhancer regions. Given that nuclear YAP condensates were enriched in YAP-specific transcription factors and co-activators, we asked whether these condensates marked super-enhancer regions. To test this, we visualized the accessible chromatin in cells using a recently developed

**Fig. 3 | Endogenous YAP form condensates.** **a**, Rapid localization of endogenous YAP to the nucleus of HEK293T cells visualized by immunofluorescence microscopy with antibody staining. The experiment was repeated four times independently with similar results. **b**, Immunofluorescence images showing the endogenous YAP in HEK293T cells form condensates in response to treatment with 0.2 M sorbitol for 10 min. The YAP signal in both diffuse and condensate form is depleted by RNAi against YAP. The experiment was repeated three times independently with similar results. **c–h**, Endogenous Halo-tagged YAP forms condensates in U-2 OS cells, visualized by Airyscan live-cell imaging. Live-cell imaging (**c**) and quantification (**d**) show that the number of nuclear Halo-YAP condensate labelled by JF549 Halo dye increases after sorbitol treatment. Two-sided paired *t*-test; *n* = 44 biologically independent samples. **e**, FRAP recovery curve of the YAP-HaloTag condensate in sorbitol-treated cells. *n* = 12 biologically independent experiments. **f**, Immunofluorescence images showing that YAP-HaloTag (labelled with JF549 Halo dye) colocalizes with endogenous YAP labelled with YAP antibody in cells treated with 10% PEG 300 for 10 min. The experiment was repeated three times independently with similar results. **g,h**, Live-cell imaging by Airyscan (**g**) and quantifications (**h**) show that YAP-RNAi knocks down the YAP-HaloTag signal in both diffuse and condensate form. Two-sided unpaired *t*-test; *n* = 45 (control) and 43 (YAP-RNAi) biologically independent samples. **i–l**, Cells from the medulla region of the mouse kidney have nuclear YAP in condensate form. **i**, Illustration of a kidney and the relative locations of the cortex and medulla. **j**, Representative YAP immunofluorescence images of mouse kidney cells in the cortex (top) and medulla (bottom) regions. A larger field of view is shown on the left; the yellow boxed regions have been magnified on the right. **k**, Nuclear to cellular ratio of YAP in the indicated regions. Two-sided unpaired *t*-test; *n* = 45 (cortical cells) and 38 (medulla cells) biologically independent samples. **l**, Number of condensates in the nuclei of kidney cells with visible condensates. Two-sided unpaired *t*-test; *n* = 36 (cortical cells) and 27 (medulla cells) biologically independent samples. The centres of the data indicate the mean and the error bars show the s.e.m. (**d,h,k,l**) or s.d. (**e**). Scale bars, 10 µm (**a,f,g**), 5 µm (**b,c,j** (right)) and 50 µm (**j** (left)). Statistics source data are provided in Source Data Fig. 3.

ATAC-based imaging method called three-dimensional (3D) ATAC photoactivated localization microscopy (ATAC-PALM)<sup>35</sup>. In this approach, Tn5 transposase is used to insert photoactivatable fluorescent DNA probes into the accessible chromatin

domains (Fig. 6a, left) and then photoactivated localization microscopy (PALM)<sup>36</sup> combined with lattice light-sheet microscopy<sup>37,38</sup> is employed to visualize the accessible chromatin regions in 3D through the entire nucleus (Fig. 6a, right).



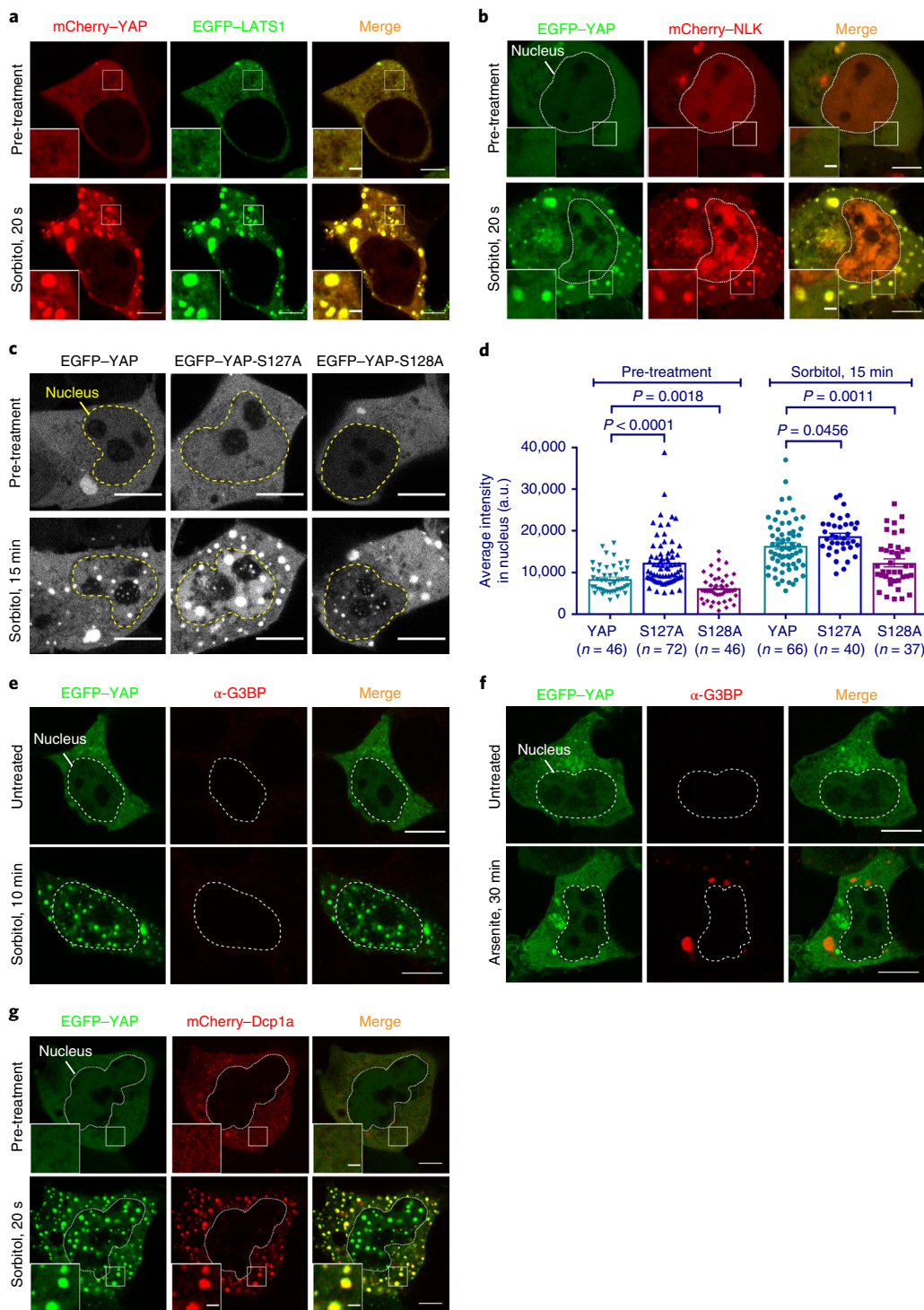


**Fig. 4 | Cytoplasmic EGFP-YAP selectively enriches different proteins.** **a**, Live-cell images showing the colocalization of mCherry-YAP condensates with EGFP-LATS1 condensates in the cytoplasm of HEK293T cells after hyperosmotic stress. The experiment was repeated three times independently with similar results. **b**, Live-cell images showing the colocalization of EGFP-YAP condensates with mCherry-NLK condensates in the cytoplasm of HEK293T cells after hyperosmotic stress. The experiment was repeated three times independently with similar results. **c,d**, Live-cell images of HEK293T cells show that wild-type and mutant EGFP-YAP are able to form condensates with sorbitol treatment (**c**), although the nuclear localization before and after sorbitol treatment changes, quantified in **d**. **d**, Comparisons were performed between the mutants and wild-type YAP using a two-sided unpaired t-test. The centre of the data indicates the mean. The number of biologically independent samples in each group is indicated. **e**, Representative immunofluorescence images showing that treatment with 0.2 M sorbitol for 10 min induces the formation of EGFP-YAP condensates in HEK293T cells but not stress-granule formation (visualized using G3BP antibody). The experiment was repeated three times independently with similar results. **f**, Representative immunofluorescence images showing that treatment with 0.5 mM arsenite for 30 min induces stress-granule formation but not YAP-condensate formation. The experiment was repeated three times independently with similar results. **g**, Live-cell images showing the colocalization of EGFP-YAP condensates with mCherry-Dcp1a condensates in the cytoplasm of HEK293T cells after hyperosmotic stress. The experiment was repeated three times independently with similar results. Scale bars, 5  $\mu$ m (**a,b,g**) (whole-cell images), 1  $\mu$ m (**a,b,g**) (magnified views of the boxed regions) and 10  $\mu$ m (**c,e,f**). Statistics source data are provided in Source Data Fig. 4.

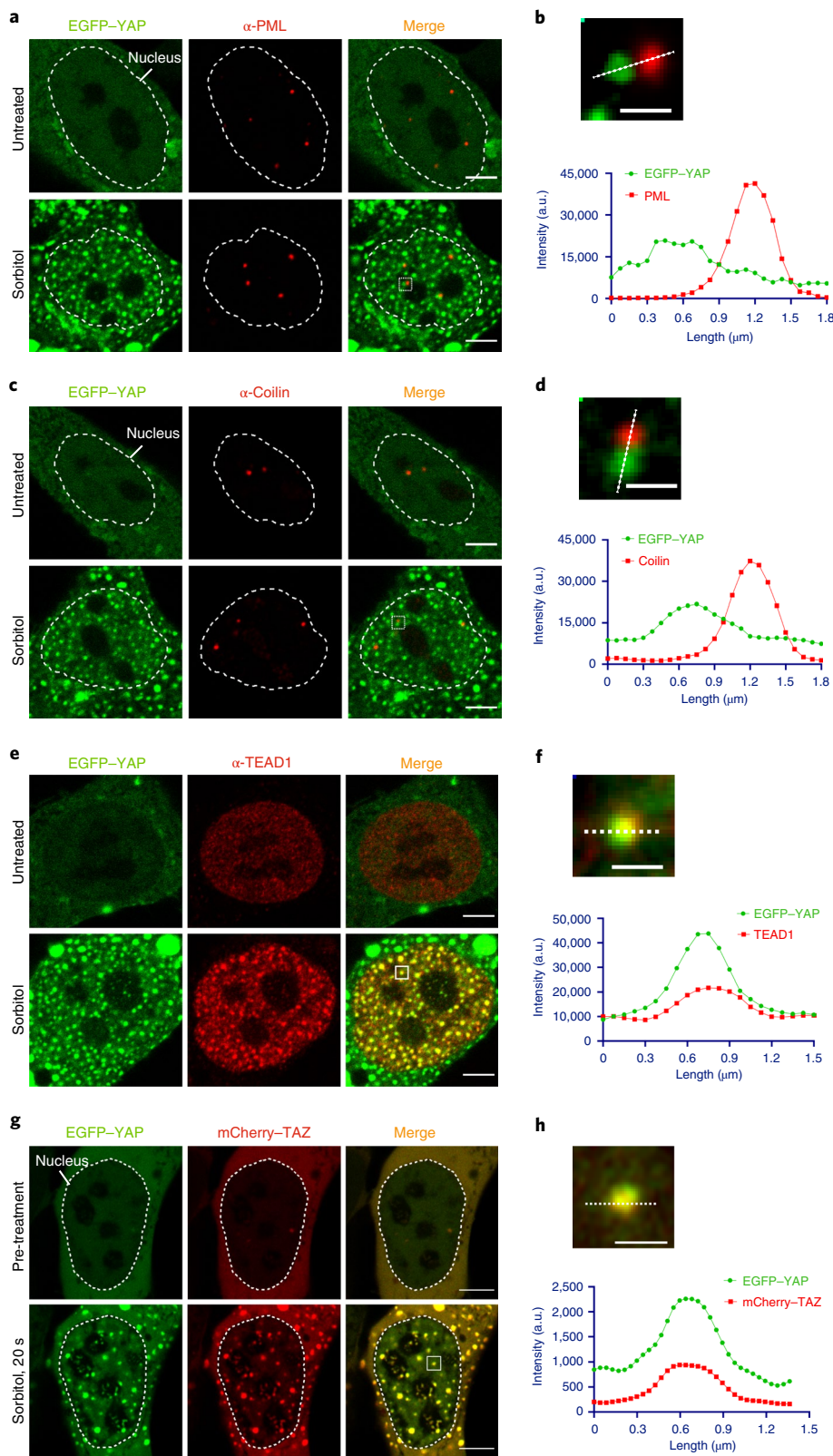


**Fig. 5 | Nuclear EGFP-YAP selectively enriches transcription-related proteins.** **a**, Immunofluorescence images showing the absence of colocalization of PML staining with EGFP-YAP before and after hyperosmotic shock. **b**, Magnification (top) of the inset in the bottom-right image of **a** and line scan of the dotted line in the magnified image (bottom). **c,d**, Similar to **a,b**. Cajal bodies (visualized using anti-coillin immunofluorescence) in HEK293T cells do not colocalize with EGFP-YAP before or after hyperosmotic shock. **e**, Immunofluorescence showing TEAD1 colocalizes with nuclear EGFP-YAP condensates under hyperosmotic stress. **f**, Magnification (top) of the boxed region in **e** and line plot of the dotted line in the magnified image (bottom). **g**, Live-cell images showing the colocalization of mCherry-TAZ with EGFP-YAP 20 s after hyperosmotic stress. **h**, Magnification (top) of the boxed region in **g** and line plot of the dotted line in the magnified image (bottom). Scale bars, 5  $\mu$ m (**a,c,e,g**) and 1  $\mu$ m (**b,d,f,h**). All of the experiments were repeated three times independently with similar results. Statistics source data are provided in Source Data Fig. 5.

ATAC-PALM imaging revealed that accessible chromatin regions were widely dispersed throughout the nucleus before hyperosmotic-shock treatment, with a few of these regions clustered into observable puncta (arrows in Fig. 6b and Supplementary Video 5). Strikingly, large ATAC-labelled clusters were seen distributed across the nucleus after 5 min of hyperosmotic treatment with sorbitol (arrows in Fig. 6c and Supplementary Video 6). Pair autocorrelation analysis—used to quantify differences in the density and size of the clustered accessible chromatin regions—revealed that the accessible chromatin regions under sorbitol treatment, on average, became significantly more clustered than before treatment (Fig. 6d). Measurements of the radii of the ATAC clusters in sorbitol-treated cells demonstrated that some clusters were more than 400 nm in diameter, which was significantly larger than control cells whose average diameter was approximately 120 nm (Fig. 6e). The significant size increase of the ATAC-labelled clusters could reflect the fusion of neighbouring accessible chromatin regions, the appearance of entirely new accessible chromatin regions, or both.

To test whether the enlarged ATAC-positive structures under sorbitol treatment represented YAP condensates, we compared the localizations of ATAC structures with EGFP-YAP condensates in sorbitol-treated cells. Remarkably, virtually all ATAC-positive structures were associated with the EGFP-YAP condensates (Fig. 6f and Supplementary Video 7). This suggested that the osmotically driven phase separation of YAP into condensates reorganizes the genome into clusters of accessible chromatin regions enriched in YAP and its binding partners.

**Nuclear YAP condensates become sites of active gene transcription.** We probed the nuclear YAP condensates with accessible chromatin domains with antibodies to RNA polymerase II (RNAPII) to determine whether these are sites of active gene transcription. RNAPII was initially segregated from the YAP nuclear droplets at 10 min of hyperosmotic shock with sorbitol (Fig. 7a,b and Extended Data Fig. 6a). However, RNAPII was no longer excluded from the YAP condensates after 2 h of sorbitol treatment. Instead, RNAPII now decorated the surface of the nuclear YAP condensates (Fig. 7c and Extended Data Fig. 6b). This suggested that while initially driving the clustering of gene-enhancer elements to form super-enhancers, the YAP nuclear condensates do not recruit RNAPII until later, presumably after the cell has had time to adapt to hyperosmotic conditions.

Given that RNAPII localizes to the surface of YAP condensates after 2 h of hyperosmotic stress, we examined the distribution of nascent RNA to determine whether the condensate sites were sites of active gene transcription. Nascent RNA did not specifically localize at clustered sites before treatment or at YAP-containing nuclear

condensates after 5 min sorbitol treatment (Fig. 7d,e). However, a large amount of nascent RNA was selectively transcribed at the clustered sites associated with nuclear YAP condensates after the cells had been in sorbitol for 2 h (Fig. 7f). The increase in expression of the YAP target gene products *Ctgf* and *Cyr61* within 3 h of sorbitol treatment, which was observed in PCR-with-reverse-transcription (RT-PCR) experiments (Fig. 2a), suggests that this leads to an increase in YAP target gene transcription.

**The intrinsically-disordered YAP TAD is responsible for YAP condensate formation and its downstream effects on transcription.** To test whether YAP condensate formation is necessary for the above effects on gene transcription, we deleted the intrinsically-disordered C-terminal TAD of YAP (generating EGFP-YAP $\Delta$ TAD; Fig. 8a). Following the expression of EGFP-YAP $\Delta$ TAD, only about 2.3% of the expressing cells formed condensates following hyperosmotic shock, compared with approximately 92.7% of cells expressing EGFP-YAP (Fig. 8b). This suggested that without its TAD sequence YAP is unable to phase separate into condensates. Notably, endogenous YAP failed to form condensates in cells expressing EGFP-YAP $\Delta$ TAD (Extended Data Fig. 7b,c), suggesting the mutant could act as a dominant negative in YAP phase condensation.

TEAD1 was not enriched in any nuclear foci in EGFP-YAP $\Delta$ TAD-expressing cells—in which YAP condensates did not form—following hyperosmotic stress (Fig. 8c). Measurements of the levels of *Ctgf* and *Cyr61* messenger RNAs 3 h after sorbitol treatment revealed a significant decrease in expression of the mRNAs in cells expressing EGFP-YAP $\Delta$ TAD compared with cells expressing EGFP-YAP (Fig. 8d). These results suggest that the intrinsically-disordered YAP TAD is responsible for YAP condensate formation and later expression of YAP target genes during sorbitol treatment.

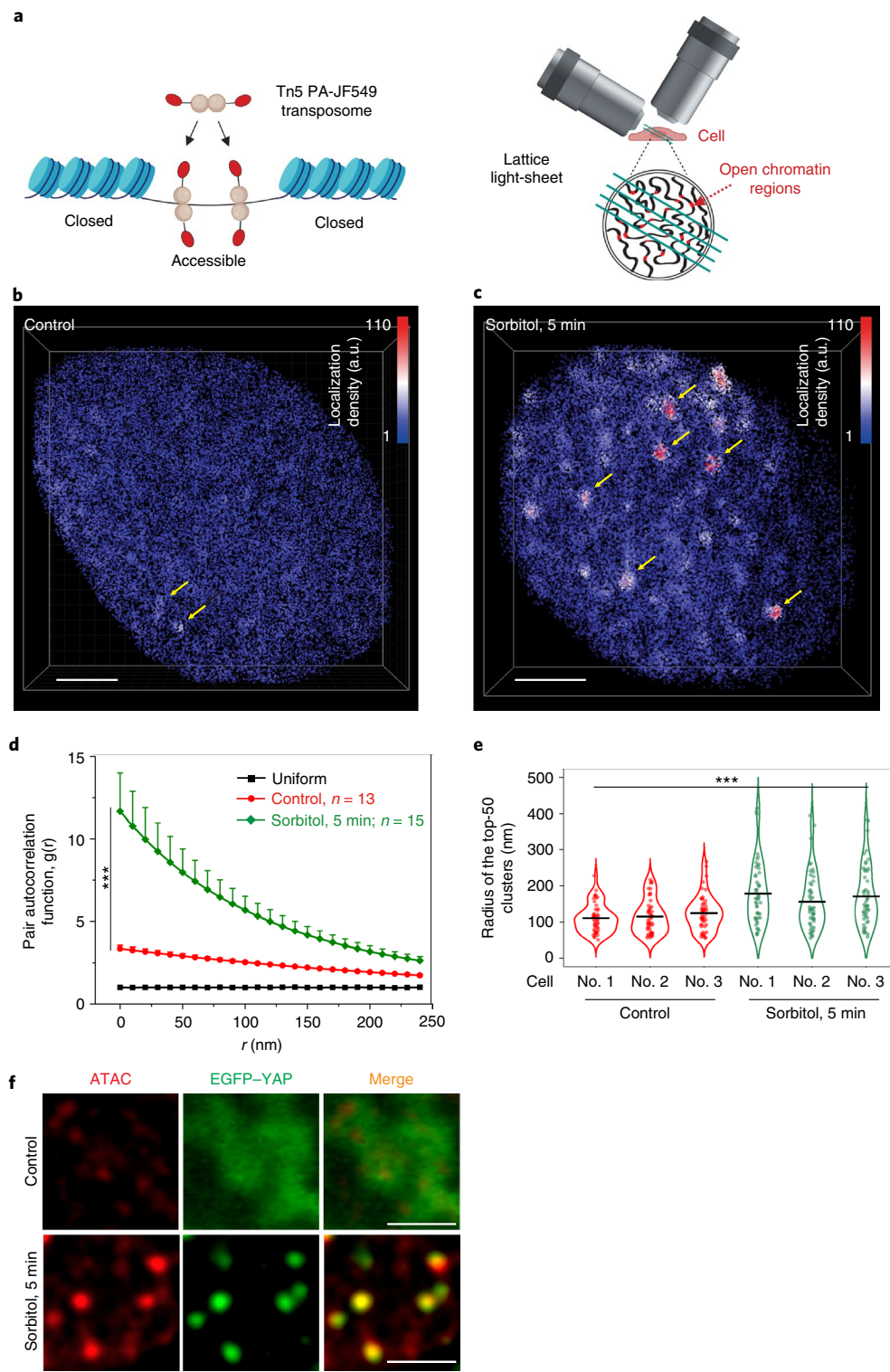
## Discussion

Our work shows that the nuclear localization and activity of YAP, a key Hippo-pathway transducer, is regulated by liquid–liquid phase separation. Specifically, the hyperosmotic stress-induced condensation of YAP into liquid droplets shifts its distribution from the cytoplasm to the nucleus, where it drives the transcription of genes involved in cell proliferation. Because the cytoplasmic and nuclear YAP droplets sequestered different sets of proteins, with cytoplasmic droplets containing NLK and nuclear droplets containing TEAD1, their formation seemed to contribute both to the ability of YAP to redistribute into the nucleus and to its role in transcriptional control. Our findings thus highlight a mechanism involving phase separation that enables YAP to collaborate with different factors in different cellular compartments to control its activity during signalling.

**Fig. 6 | YAP condensates induced by sorbitol treatment alter the 3D organization of accessible chromatin.** **a**, Schematics of the 3D ATAC-PALM microscopy labelling and imaging strategy. Photoactivatable Janelia Fluor 549 (PA-JF549) was conjugated to a DNA oligo containing the mosaic ends of the Tn5 transposon and reconstituted with Tn5 transposase (cyan) to form the active transposome complex in vitro (left). The cells were then fixed and permeabilized, and the accessible sites in the genome were selectively labelled by the reconstituted active transposome complex before mounting onto the lattice light-sheet microscope for 3D ATAC-PALM imaging (right). **b,c**, 3D ATAC-PALM images of the accessible chromatin localizations in control (**b**) and sorbitol-treated (**c**) HEK293T cells. The colour-coded localization density was calculated with a canopy radius of 250 nm. The yellow arrows point to the identified ATAC clusters. **d**, Global pair autocorrelation function ( $g(r)$ ) analysis of the ATAC-PALM localizations for control and sorbitol-treated HEK293T cells. The  $g(r)$  was plotted from the fitted exponential decay function. The centres of the data represent the mean and the error bars indicate the s.e.m. \*\*\* $P=1.49\times 10^{-5}$ ; the non-parametric two-sided Mann-Whitney U-test was used to compare the clustering amplitude A (equal to  $g(0)$ ) between different groups;  $n=13$  (control) and 15 (sorbitol-treated) biologically independent cells. **e**, Normalized radii of the top-50 identified accessible chromatin clusters, identified using the DBSCAN algorithm, in control and sorbitol-treated HEK293T cells. The radius of each cluster was plotted as a dot and the violin plot shows the distribution of these 50 data points. The bars indicate the median values of each group;  $n=10$  biologically independent samples. \*\*\* $P=2\times 10^{-8}$ ; the data from three individual cells for each condition were pooled and a two-sided Mann-Whitney U-test was applied for statistical analysis. **f**, Representative images show the colocalization of the identified accessible chromatin clusters and YAP condensates in control and sorbitol-treated HEK293T cells. To derive the ATAC-PALM intensity map (red) for comparison to the EGFP-YAP signal, the ATAC-PALM localizations were binned within a cubic of 100 nm with a 3D Gaussian filter and a convolution kernel of  $3\times 3\times 3$ . The experiments were repeated three times independently with similar results. Scale bars, 2  $\mu$ m. Statistics source data are provided in Source Data Fig. 6.

The Hippo signalling pathway governs tissue growth and homeostasis by regulating cell proliferation and differentiation, with control of these cellular processes occurring through the pathway-mediated localization of the downstream effectors YAP/TAZ. The overall activity of Hippo signalling is to prevent the transcriptional activity of the downstream effectors of YAP and TAZ, which is accomplished by the retention of these transcription cofactors in the cytoplasm through the activity of a cascade of core kinases (including the kinases MST1/2 and LATS1/2). Although many signals activate the

Hippo pathway (that is, by the engagement of receptors that activate the core kinases), the events that antagonize the pathway have only begun to be understood. One antagonizing event is the phosphorylation of YAP at Ser128 by NLK, which occurs in response to hyperosmotic stress and leads to YAP redistribution into the nucleus<sup>6</sup>. Our finding that NLK colocalizes with YAP in cytoplasmic droplets under hyperosmotic stress suggests this co-compartmentalization serves to rapidly alter the phosphorylation kinetics of YAP through increased kinase and substrate concentrations in the droplet. The



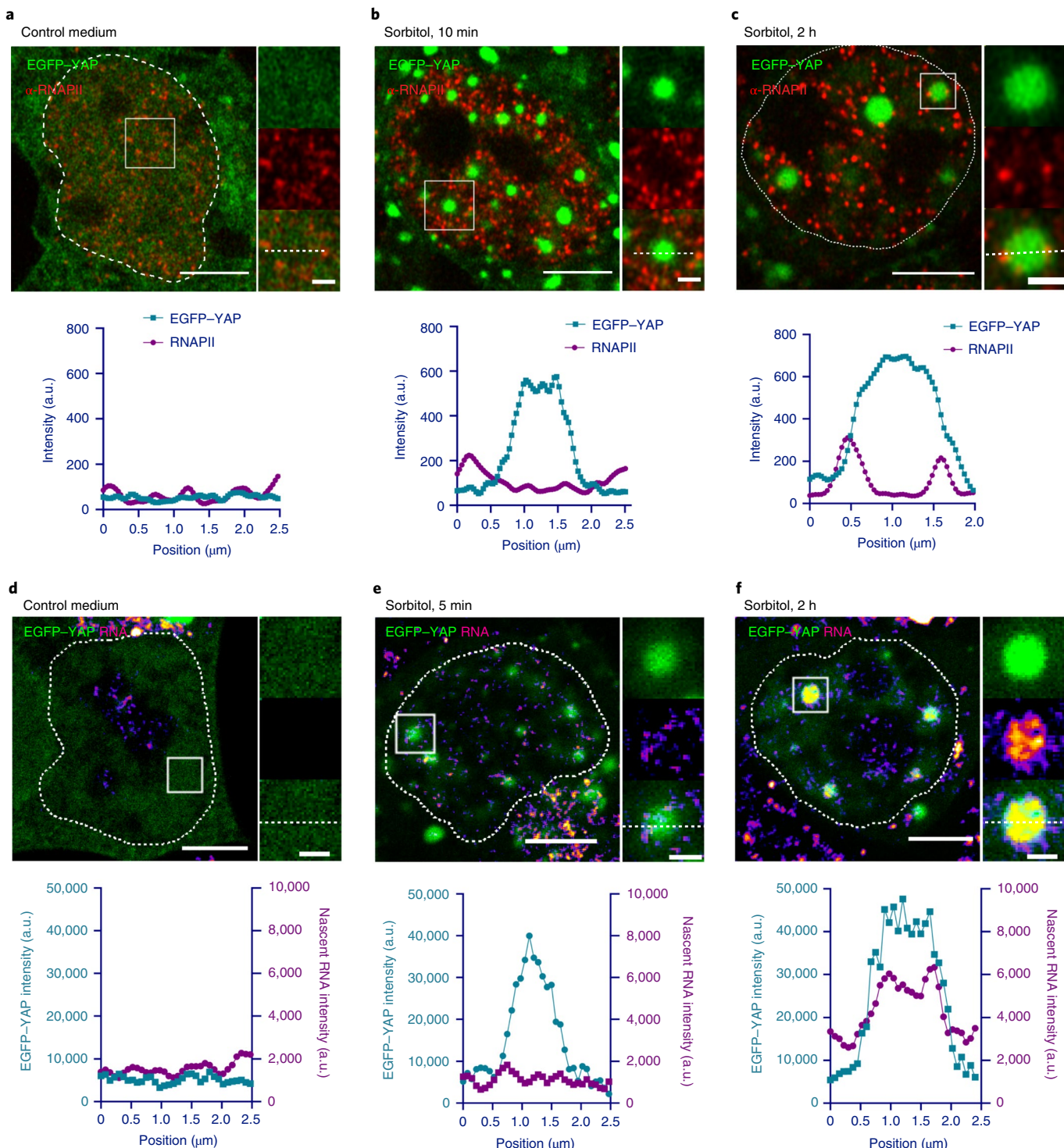


**Fig. 7 | EGFP-YAP nuclear condensate localization with RNAPII during sorbitol treatment.** **a–c**, Immunofluorescence images (top) and line plots (bottom) of the indicated regions (dashed lines) showing the localization of EGFP-YAP and RNAPII (pSer2) under different conditions. **d–f**, Localization of EGFP-YAP and nascent RNA, pulse-labelled with 5-ethynyl uridine for 5 min and visualized using Click-iT chemistry. The RNA is shown in the Fire look-up table from ImageJ (top). Line plots of the EGFP-YAP condensate localization and nascent RNA signal (bottom). Scale bars, 5  $\mu\text{m}$  (whole-nucleus views, left) and 1  $\mu\text{m}$  (condensate views, right). All of the experiments were repeated three times independently with similar results. The numerical source data are provided in Source Data Fig. 7.

additional presence of LATS1 in YAP cytoplasmic droplets could serve to modulate this effect, as we observed decreased pools of YAP in the nucleus in LATS1-overexpressing cells. The sequestration of YAP into cytoplasmic condensates under hyperosmotic stress

could help prevent YAP from interacting with 14-3-3 proteins, such as the 14-3-3 $\sigma$  protein. In addition, cytoplasmic YAP condensates could protect YAP from targeted degradation by phosphorylated casein kinase in the cytoplasm<sup>39</sup>. Understanding how these and

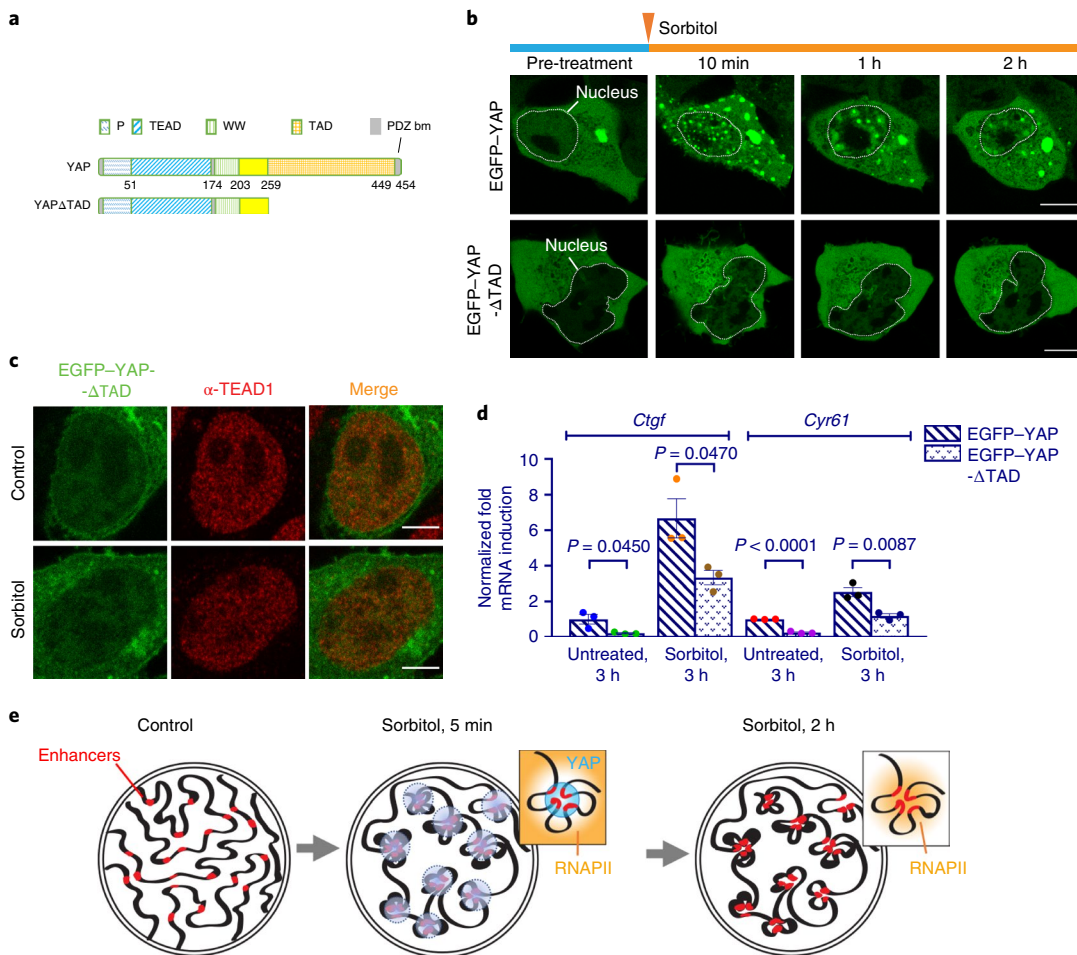


**Fig. 8 | Phase separation of YAP is important for its nuclear localization and signalling.** **a**, Illustration of wild-type YAP (isoform 3; UniProt identifier: P46937-3) and YAP $\Delta$ TAD structures. The numbers show the amino acid position in the wild-type YAP. **b**, Live-cell images showing the time-dependent phase separation of EGFP-YAP variants in HEK293T cells. **c**, Immunofluorescence images of the relative localization of EGFP-YAP $\Delta$ TAD with TEAD1 in control or 0.2 M sorbitol-treated HEK293T cells. The experiment was repeated three times independently with similar results. **d**, Relative expression levels of *Ctgf* and *Cyr61* mRNA, quantified through RT-PCR, in HEK293T cells expressing EGFP-YAP variants after the indicated treatments. The centre of the data is the mean and the error bars show the s.e.m.; two-sided unpaired *t*-test;  $n=3$  biologically independent experiments. **e**, Model depicting the remodelling of enhancer elements by YAP phase separation. Scale bars, 10  $\mu$ m (**b**) and 5  $\mu$ m (**c**). Statistics source data are provided in Source Data Fig. 8.

other core Hippo kinase members—including MST1/2, PP2A, Sav1 and MOB1—distribute and behave when YAP droplets form under hyperosmotic stress is an important area for future work as their modulation could be relevant in therapeutic studies.

Another area impacted by our findings relates to nuclear reorganization by YAP condensates. A growing body of work that includes light-induced phase-separation systems<sup>40–42</sup> suggests the importance of phase separation in reorganizing the genome for transcription<sup>12–15</sup>. Our finding of the osmotically driven assembly and later disassembly of YAP nuclear condensates provides a physiologically relevant approach for the analysis of condensate-induced changes in nuclear organization. Indeed, by using the ATAC-PALM super-resolution imaging method to visualize accessible chromatin regions, we found that the genome of the cell reorganized dramatically within 5 min of hyperosmotic stress. During this interval, the dispersed accessible chromatin domains observed in untreated cells became highly concentrated in large YAP-containing nuclear condensates.

Canonically, YAP binds to TEAD family members to induce the transcription of YAP target genes. However, how the targeted genomic loci are coordinately controlled remains unclear. YAP constructs incapable of condensate formation (that is, YAP $\Delta$ TAD)

prevented both TEAD1 localization to clusters and the expression of YAP target genes during hyperosmotic stress, suggesting that the presence of YAP condensates during hyperosmotic stress is functionally relevant for YAP signalling. We found TEAD1, TAZ and accessible chromatin regions colocalize with newly formed YAP droplets within minutes of hyperosmotic stress. This raises the possibility that YAP nuclear condensates physically pull in the targeted genomic loci while pushing out non-targeted regions of the neighbouring genome to allow for the synchronized transcription of YAP target genes, a characteristic of nuclear condensates that has been proposed by others<sup>12,13,15,41</sup>. During this genome reorganization, we observed that although RNAPII was initially excluded from the YAP droplets, it later became localized at the rim of the droplets, as did newly transcribed RNA. This coincided with the expression of YAP downstream target genes in these cells. Therefore, YAP nuclear condensates dynamically restructure the overall genomic environment over time (Fig. 8e).

In summary, we have shown that the distinct localizations/functions of YAP in the cytoplasm and nucleus can be controlled by its ability to undergo phase condensation in response to hyperosmotic stress. This allows YAP to be a sensor of mechanical forces in tissues that cause changes in macromolecular crowding. Additional

strategies for the modification of YAP target gene expression may thus become possible to alter the course of cancer and other diseases involving YAP signalling—for example, through droplet disruptors or reagents that change macromolecular crowding.

## Online content

Any methods, additional references, Nature Research reporting summaries, source data, extended data, supplementary information, acknowledgements, peer review information, details of author contributions and competing interests, and statements of code and data availability are available at <https://doi.org/10.1038/s41556-019-0433-z>.

Received: 14 October 2018; Accepted: 30 October 2019;

Published online: 2 December 2019

## References

- Pan, D. The Hippo signaling pathway in development and cancer. *Dev. Cell* **19**, 491–505 (2010).
- Zanconato, F., Cordenonsi, M. & Piccolo, S. YAP/TAZ at the roots of cancer. *Cancer Cell* **29**, 783–803 (2016).
- Lian, I. et al. The role of YAP transcription coactivator in regulating stem cell self-renewal and differentiation. *Genes Dev.* **24**, 1106–1118 (2010).
- Dupont, S. et al. Role of YAP/TAZ in mechanotransduction. *Nature* **474**, 179–183 (2011).
- Deran, M. et al. Energy stress regulates Hippo-YAP signaling involving AMPK-mediated regulation of angiomotin-like 1 protein. *Cell Rep.* **9**, 495–503 (2014).
- Hong, A. W. et al. Osmotic stress-induced phosphorylation by NLK at Ser128 activates YAP. *EMBO Rep.* **18**, 72–86 (2017).
- Shin, Y. & Brangwynne, C. P. Liquid phase condensation in cell physiology and disease. *Science* **357**, eaaf4382 (2017).
- Banani, S. F., Lee, H. O., Hyman, A. A. & Rosen, M. K. Biomolecular condensates: organizers of cellular biochemistry. *Nat. Rev. Mol. Cell Biol.* **18**, 285–298 (2017).
- Jain, A. & Vale, R. D. RNA phase transitions in repeat expansion disorders. *Nature* **546**, 243–247 (2017).
- Strom, A. R. et al. Phase separation drives heterochromatin domain formation. *Nature* **547**, 241–245 (2017).
- Larson, A. G. et al. Liquid droplet formation by HP1α suggests a role for phase separation in heterochromatin. *Nature* **547**, 236–240 (2017).
- Sabari, B. R. et al. Coactivator condensation at super-enhancers links phase separation and gene control. *Science* **361**, eaar3958 (2018).
- Boija, A. et al. Transcription factors activate genes through the phase-separation capacity of their activation domains. *Cell* **175**, 1842–1855 (2018).
- Cho, W. K. et al. Mediator and RNA polymerase II clusters associate in transcription-dependent condensates. *Science* **361**, 412–415 (2018).
- Hnisz, D., Shrinivas, K., Young, R. A., Chakraborty, A. K. & Sharp, P. A. A phase separation model for transcriptional control. *Cell* **169**, 13–23 (2017).
- Hnisz, D. et al. Super-enhancers in the control of cell identity and disease. *Cell* **155**, 934–947 (2013).
- Galli, G. G. et al. YAP drives growth by controlling transcriptional pause release from dynamic enhancers. *Mol. Cell* **60**, 328–337 (2015).
- Zanconato, F. et al. Transcriptional addiction in cancer cells is mediated by YAP/TAZ through BRD4. *Nat. Med.* **24**, 1599–1610 (2018).
- Lin, Y., Prottier, D. S. W., Rosen, M. K. & Parker, R. Formation and maturation of phase-separated liquid droplets by RNA-binding proteins. *Mol. Cell* **60**, 208–219 (2015).
- Smith, J. et al. Spatial patterning of P granules by RNA-induced phase separation of the intrinsically-disordered protein MEG-3. *eLife* **5**, e21337 (2016).
- Alberti, S., Gladfelter, A. & Mittag, T. Considerations and challenges in studying liquid-liquid phase separation and biomolecular condensates. *Cell* **176**, 419–434 (2019).
- Gottschalk, C. W. & Mylle, M. Micropuncture study of the mammalian urinary concentrating mechanism: evidence for the countercurrent hypothesis. *Am. J. Physiol.* **196**, 927–936 (1959).
- Wirz, H. Kidney, water and electrolyte metabolism. *Annu. Rev. Physiol.* **23**, 577–606 (1961).
- Guyton, A. & Hall, J. in *Textbook of Medical Physiology* (ed Hall, J) 349–365 (Elsevier Saunders, 2006).
- Jamison, R. L. & Maffly, R. H. The urinary concentrating mechanism. *New Eng. J. Med.* **295**, 1059–1067 (1976).
- Dong, J. X. et al. Elucidation of a universal size-control mechanism in *Drosophila* and mammals. *Cell* **130**, 1120–1133 (2007).
- Hao, Y. W., Chun, A., Cheung, K., Rashidi, B. & Yang, X. L. Tumor suppressor LATS1 is a negative regulator of oncogene YAP. *J. Biol. Chem.* **283**, 5496–5509 (2008).
- Moon, S. et al. Phosphorylation by NLK inhibits YAP-14-3-3-interactions and induces its nuclear localization. *EMBO Rep.* **18**, 61–71 (2017).
- Vassilev, A., Kaneko, K. J., Shu, H., Zhao, Y. & DePamphilis, M. L. TEAD/TEF transcription factors utilize the activation domain of YAP65, a Src/Yes-associated protein localized in the cytoplasm. *Genes Dev.* **15**, 1229–1241 (2001).
- Zhao, B. et al. TEAD mediates YAP-dependent gene induction and growth control. *Genes Dev.* **22**, 1962–1971 (2008).
- Wu, T. et al. Phase separation of TAZ compartmentalizes the transcription machinery to promote gene expression. Preprint at *bioRxiv* <https://doi.org/10.1101/671230> (2019).
- Boyle, A. P. et al. High-resolution mapping and characterization of open chromatin across the genome. *Cell* **132**, 311–322 (2008).
- Wu, C. The 5' ends of *Drosophila* heat shock genes in chromatin are hypersensitive to DNase I. *Nature* **286**, 854–860 (1980).
- Buenrostro, J. D., Giresi, P. G., Zaba, L. C., Chang, H. Y. & Greenleaf, W. J. Transposition of native chromatin for fast and sensitive epigenomic profiling of open chromatin, DNA-binding proteins and nucleosome position. *Nat. Methods* **10**, 1213–1218 (2013).
- Xie, L. et al. Super-resolution imaging reveals 3D structure and organizing mechanism of accessible chromatin. Preprint at *bioRxiv* <https://doi.org/10.1101/678649> (2019).
- Betzig, E. et al. Imaging intracellular fluorescent proteins at nanometer resolution. *Science* **313**, 1642–1645 (2006).
- Chen, B. C. et al. Lattice light-sheet microscopy: imaging molecules to embryos at high spatiotemporal resolution. *Science* **346**, 1257998 (2014).
- Legant, W. R. et al. High-density three-dimensional localization microscopy across large volumes. *Nat. Methods* **13**, 359–365 (2016).
- Zhao, B., Li, L., Tumaneng, K., Wang, C. Y. & Guan, K. L. A coordinated phosphorylation by Lats and CK1 regulates YAP stability through SCF<sup>β-TRCP</sup>. *Gene Dev.* **24**, 72–85 (2010).
- Shin, Y. et al. Spatiotemporal control of intracellular phase transitions using light-activated optoDroplets. *Cell* **168**, 159–171 (2017).
- Shin, Y. et al. Liquid nuclear condensates mechanically sense and restructure the genome. *Cell* **175**, 1481–1491.e13 (2018).
- Bracha, D. et al. Mapping local and global liquid phase behavior in living cells using photo-oligomerizable seeds. *Cell* **175**, 1467–1480 (2018); erratum **176**, 407–407 (2019).

**Publisher's note** Springer Nature remains neutral with regard to jurisdictional claims in published maps and institutional affiliations.

© The Author(s), under exclusive licence to Springer Nature Limited 2019

## Methods

**Constructs.** The plasmids pEGFP-C3-hYAP1 (Addgene, cat. no. 17843) and pEGFP-C3-Mst2 (Addgene, cat. no. 19056) were gifts from M. Sudol. The mCherry-Dcp1a was a gift from P.-W. Lau. To construct mCherry–NLK, NLK was first PCR amplified from the pDONR223–NLK plasmid (a gift from W. Hahn and D. Root; Addgene, cat. no. 23642) using the primers 5'-CTCAAGCTTCGAATTCTGCACTTCCACACCTCCCTCCTC-3' and 5'-GATCCGGTGGATCCGGCCCTCCACACCAGAGGAGATG-3', and pmCherry–C1 (Clonetech) was PCR amplified using 5'-GGCCCCGGAT CCACCGGA-3' and 5'-TGCAGAATTCTGAAAGCTTGAGCTC-3'. The amplified NLK and mCherry–C1 fragments were then assembled using the NEBuilder HiFi DNA assembly master mix. For the construction of pET28b–YAP, the plasmids pET28b (+) (EMD Millipore) and pEGFP-C3-hYAP1 were both double-digested with NheI and EcoRI (NEB) and ligated together using T4 DNA ligase. Subsequently, EGFP–YAP was brought in-frame with 6xHis–thrombin using the QuikChange lightning site-directed mutagenesis kit (Agilent, cat. no. 210519) and the primers 5'-GCTACCCGGTCGCCACATGGTGGAGCAAGG-3' and 5'-CCTTGCTCACCATGTGGCGACCGGGTAGC-3'. For the generation of the YAP truncations, pEGFP-C3-hYAP1 (Addgene, cat. no. 17843) was used as a template to amplify YAP-ΔTAD (FWR, 5'-GGAAGATCTTCCATGGATCCC GGGCAGCAG-3' and REV, 5'-CCGGAAATTCCGGCTAACCCATGACG CCTCCCTG-3') by PCR and then these were cloned into the BglII/EcoRI sites of pEGFP-C3. To generate the pEGFP–YAP-S127A and pEGFP–YAP-S128A constructs, the pEGFP-C3-hYAP1 construct was used as a template and the QuikChange lightning site-directed mutagenesis kit was used to generate point mutations using the following primers: 5'-GAGAACGCTGGAGAGGCATGAG CTCGAACATGCT-3' (forward) and 5'-AGCATGTTGAGCTCATGCCT CCTCCAGCTCTC-3' (reverse) for S127A, and 5'-GTTCGAGCTATTCCG CTCCAGCTCTGAGCT-3' (forward), 5'-GCAGAGAAGCTGGAGCG GAATGAGCTCGAACATGCT-3' (reverse) for S128A.

**In vitro EGFP–YAP expression, protein purification and phase-separation experiments.** The pET28b–EGFP–YAP plasmid was used to transform *E. coli* BL21 DE3 RIPL cells (Invitrogen) using the standard supplier protocol. The cells were grown to an optical density ( $OD_{600}$ ) of 0.6, lysed using a tip sonicator and purified by His-tag affinity chromatography on a GE-Healthcare AKTA system. The purified protein was concentrated to approximately 1 mg ml<sup>-1</sup> and run on a Sephadex 200 size-exclusion column in 20 mM Tris pH 8.0. The collected fractions contained the clean protein, as verified with SDS-PAGE and matrix-assisted laser desorption/ionization time-of-flight mass spectrometry. The phase-separation conditions were assessed by sample turbidity, measured as the  $OD_{600}$  of EGFP–YAP solutions in 96-well clear-plastic plates using a Molecular Designs SpectraMax plate reader. To determine the partition coefficient  $K_p$  of YAP (Fig. 3i) between solution and protein-rich droplets, phase-separation reactions were prepared in 1.5 ml tubes with 40  $\mu$ M EGFP–YAP, different PEG sizes (Sigma) at concentrations ranging from 0 to 35% (w/w) and 20 mM Tris buffer, pH 8.0. At given times, the reaction solution was gently stirred and a 50  $\mu$ l aliquot was removed. The aliquot was spun down at maximum speed for 15 min. A bright-green pellet was observed on the bottom of the tubes, and the supernatant was carefully removed, diluted 5× in Tris buffer and placed in a 96-well plate for absorbance measurements at the maximal absorbance wavelength of EGFP (488 nm). The concentration of EGFP–YAP in the soluble phase was estimated based on the EGFP absorbance.

Confocal imaging of purified EGFP–YAP was done on an LSM880 microscope equipped with an Ar laser line. Imaging chambers were prepared on clean glass slides using a 120- $\mu$ m double-sided sticker (Grace Biolabs), and sealed with a 1.5 coverslip. Imaging was done on a single slice, with the pinhole opened to 2 Airy units.

**Cell culture, transfection, siRNA and live-cell imaging.** U-2 OS (gift from L. Chen) and HEK293T (gift from the A. Banerjee lab) cells were cultured at 37 °C and 5% CO<sub>2</sub> in complete medium: DMEM supplemented with 10% fetal bovine serum (FBS; Gibco), 100 U ml<sup>-1</sup> penicillin/streptomycin (Corning) and 2 mM L-glutamine (Corning). No International Cell Line Authentication Committee cell lines were used in this study. For confocal imaging, the cells were cultured on eight-well LabTek chambered coverglass dishes (Thermo Scientific) and transfected using Lipofectamine 3000 reagent (Thermo Fisher). The cells were imaged 18 h after transfection on a Zeiss LSM780 confocal microscope at room temperature with plan-apochromat  $\times$ 63/1.40 oil objective. For the RNAi experiments, YAP siRNA (Thermo Fisher, Silencer Select s20367) or negative control (Thermo Fisher, AM4611) was transfected into cells (pre-seeded on six-well plates) using the Lipofectamine RNAiMAX transfection reagent (Thermo Fisher, cat. no. 13778075). After transfection (48 h), the cells were replated onto six-well plates to confirm knockdown by immunoblotting or to eight-well LabTek chambered coverglass dishes for imaging on the following day. Images were taken every 30 s in a z-stack of three slices with an interval of 0.4  $\mu$ m. For the volume measurements, cells pre-transfected with EGFP–YAP were labelled with Hoechst 33342 (Thermo Fisher, cat. no. 62249) for 30 min before confocal imaging. Dual-colour imaging and z-sectioning was done across the whole-cell and nuclear volume, with an interval of 0.5  $\mu$ m. The cell and nuclear volume measurements were done with the Imaris software (Bitplane) using the surface reconstruction

tool and the cytoplasmic volume was calculated by subtracting the nuclear volume (Hoechst channel) from the cell volume (EGFP channel). Images were taken every 4.5 s with Definite Focus to visualize the fusion of the YAP condensates. Zoomed-in images were smoothed once using ImageJ for display.

**Fluorescence recovery after photobleaching (FRAP).** HEK293T cells expressing EGFP–YAP were treated with 0.2 M sorbitol, and FRAP experiments were done on cytoplasmic or nuclear YAP condensates formed immediately after treatment using the bleaching mode in Zen. The region of interest was selected on either the entire condensate or part of it using a rectangular box of approximately 1  $\mu$ m  $\times$  1  $\mu$ m in size. Twenty iterations of bleaching were done with a 488 nm Argon laser at 100% power. Five and 300 rounds of imaging were performed before and after bleaching until fluorescence signal plateau, respectively, with an interval of 450 ms. The  $t_{1/2}$  was calculated using the FRAP module in Zen software, with the fit formula for one diffusion component.

**RT-PCR.** HEK293T cells were serum-starved for 1 h and subjected to control serum-free medium or 0.2 M sorbitol serum-free medium, according to the methods described by Hong and colleagues<sup>6</sup>. The total RNA was isolated from HEK293T cells using a QIAgen RNeasy mini kit (cat. no. 74104) and converted to complimentary DNA using the Thermo Fisher high-capacity cDNA reverse transcription kit (cat. no. 4368814). The RT-PCR was carried on an Agilent AriaMx 96 real-time PCR system using Platinum SYBR green qPCR supermix-UDG (Thermo Fisher, cat. no. 11733038). The following primers were used: Gapdh, 5'-CTCTCTGACCACCAACTGCT-3' (forward) and 5'-GGGCC ATCCACAGTCTCTG-3' (reverse); Ctgf, 5'-AGGAGTGGGTGTGACGA-3' (forward) and 5'-CCAGGCAGTGGCTCTAATC-3' (reverse); Cyr61, 5'-CCTC GGCTGGTCAAAGTTAC-3' (forward) and 5'-TTTCTCGTCAACTCCACCTC-3' (reverse). The mRNA levels were normalized to those of Gapdh.

**Generation of YAP–HaloTag CRISPR knock-in U-2 OS cell line.** Single-guide RNA targeting  $\pm$ 100 bp around the stop codon of the *Yap* gene was designed using the web-based CRISPR design tool (<http://crispr.mit.edu>). One guide (TACATGTTATAGAGCCCTC) was chosen as it spans the stop codon and due to its high score. DNA oligonucleotides with BbsI restriction sites were ordered from Integrated DNA Technologies. The pSpCas9(BB)-2A-GFP (PX458) vector (Addgene, cat. no. 48138; a gift from F. Zhang)<sup>43</sup> was digested using BbsI and ligated with annealed genomic RNA (gRNA) fragment to form the *Yap* gRNA–Cas9 plasmid.

The homology repair fragment spanning the *Yap* stop codon (approximately 800 bp on either side) and containing the Halo protein-coding gene was synthesized using gBlock (Integrated DNA Technologies). The gBlock sequence is in Supplementary Note 2. The pUC57-mini vector (GenScript) was linearized with the EcoRV restriction enzyme and ligated with a Halo homology repair fragment using the NEBuilder HiFi DNA assembly master mix (NEB, E2621). All plasmids were sequence-verified by Eurofins Genomics.

The *Yap* gRNA–Cas9 and Halo-homology-repair constructs were cotransfected into U-2 OS cells using Lipofectamine 3000 transfection reagent (Thermo Fisher, L3000015). The GFP-positive cells were selected 48 h after transfection using FACS (National Eye Institute Flow Cytometry Core). The cells were grown for an additional week and stained with 100 nM JF549 Halo dye (a gift from L. Lavis, HHMI Janeia Research Campus) for 30 min, washed three times with 1×PBS, and sorted by FACS a second time for Halo-dye-positive and GFP-negative cells. Individual cells were cultured for one week in single wells of a 96-well dish supplemented with 20% FBS DMEM medium to allow positive clones to form. Cell clones were observed in 40% of the wells. The correct genome insertion was verified by genome DNA extraction (QuickExtract DNA Extraction Solution; Lucigen, QE09050) and PCR using the following primers spanning the homology arms and HaloTag: 5'-ATTCCTGGGACAAATGTGGACCTG-3' (forward) and 5'-TCAGGTCTGGAGCAATGCGAGCGATG-3' (reverse); and 5'-TGAATCCTGTTGACCGCGAGGCCATG-3' (forward), 5'-TAGAATTCTAGTCTGCCTGAGGGCTC-3' (reverse). An increase in the size of the YAP protein marked by Halo was further confirmed by immunoblotting with anti-YAP antibody (1:150; Cell Signaling, 14074S).

**Live-cell imaging of the U-2 OS YAP–HaloTag cell line.** The YAP–HaloTag U-2 OS cells were pre-plated on eight-well LabTek chambered coverglass dishes for at least 16 h in complete medium. Before imaging, the cells were incubated with complete medium containing 100 nM JF549 Halo dye for 30 min and then wash three times with 1×PBS before changing back to complete medium. The complete medium and 1×PBS need to be isotonic (old medium from which water has evaporated should not be used) to prevent the early formation of YAP–HaloTag condensates. Imaging was performed on a Zeiss LSM880 scope with Airyscan (Super-resolution mode), using a plan-apochromat  $\times$ 63/1.4 oil DIC M27 objective. A 561 nm laser, kept below 0.7% power to minimize photobleaching, was used to excite the Halo dye. The pinhole was kept at 132  $\mu$ m and the pixel sizes were 35 nm  $\times$  35 nm.

**Mice.** Eight-week-old female (FVB/NJ) mice were purchased from The Jackson Laboratory (<https://www.jax.org>) and housed at the National Institutes of Health/National Cancer Institute mice facility 10/ACRF in accordance with the NIH/NCI

regulations for the use of mice in experimental research. All procedures were performed according to protocols (LCMB-037) approved by the veterinary authorities at the NIH/NCI. The study was compliant with all of the relevant ethical regulations regarding animal research.

**Kidney dissection and immunofluorescence.** Kidney tissues from two wild-type mice were immersion-fixed with 4% paraformaldehyde (PFA) in PBS for 48 h at 4 °C. For the immunofluorescence microscopy stainings, the fixed kidney tissue was mounted in 5% low-melting agarose in PBS and sectioned into 75-μm-thick slices using a vibratome (Leica). The floating sections were permeabilized in 0.5% Triton X-100 in PBS for 1 h and blocked by incubation with blocking buffer (20% FBS and 0.2% Triton X-100 in PBS) for 2 h. The sections were incubated sequentially with a primary antibody against YAP (1:50; Cell Signaling) in blocking buffer for 72 h, washed six times with 0.2% Triton X-100 in PBS for 10 min, incubated with the secondary antibody labelled with Alexa Fluor 488 (1:500), Hoechst (1:5,000) and Alexa Fluor 568-conjugated phalloidin (1:150) in blocking buffer overnight, and washed another six times with 0.2% Triton X-100 in PBS for 10 min. The stained sections were incubated overnight in 50% glycerol and then mounted on slides in 80% glycerol. The fixed kidney samples were imaged using a Leica SP8 laser scanning confocal microscope (DMI8-CS) with a  $\times 63/1.4$  oil objective; 405, 488 and 552 laser lines and HyD detectors. Images of the kidney cortex and medulla were acquired.

**Immunofluorescence and nascent-RNA pulse labelling.** HEK293T cells were plated on coverslips pre-coated with fibronectin (7.5 μg ml<sup>-1</sup>; Millipore, FC010) for 16 h before being fixed with 4% PFA (EM5), permeabilized with 0.5% Triton X-100 and blocked with 3% BSA in 1×PBS. The cells were next incubated overnight with primary antibodies in 1% BSA at 4 °C, and then incubated with Alexa Fluor-conjugated secondary antibodies. The following primary antibodies were used: anti-YAP (1:150; Cell Signaling, 14074S, lot 4), anti-TEAD1 (1:200; BD Biosciences, cat. no. 610922, lot 6228876), anti-RNAPII CTD repeat YSPTSPS (phospho S2; 1:150; Abcam, ab193468), anti-G3BP1 (1:5,000; Proteintech, 13057-2-AP), anti-PML (1:500; Abcam, ab96051, lot GR3174201-1) and anti-coilin (1:200; Abcam, ab87913, lot GR50257-4). The nascent RNA was labelled using a Click-iT RNA Alexa Fluor 594 imaging kit (Thermo Fisher, C10330). All of the samples were transiently labelled with 2.5 mM 5-ethynyl uridine for 5 min before fixation with 4% PFA. Specifically, samples treated with 5 min sorbitol were supplemented with 0.2 M sorbitol with 2.5 mM 5-ethynyl uridine for 5 min. Samples treated with sorbitol for 2 h were supplemented with 0.2 M sorbitol for 1 h 55 min before changing to 0.2 M sorbitol supplemented with 2.5 mM 5-ethynyl uridine and incubated for 5 min. Each sample was incubated with GFP-Booster\_Atto488 (ChromoTek, gba488-100) after fixation and permeabilization, before performing Click chemistry to visualize 5-ethynyl uridine following the manufacturer's instructions. For imaging and quantification, at least 15 fields of view per coverslip were randomly chosen by Hoechst nuclear staining and imaged using a Zeiss LSM780 or LSM880 confocal microscope, or Airyscan. At least three different coverslips were quantified per treatment type.

**Colocalization.** Colocalization of two channels were done using the ImageJ Coloc 2 plugin. The region of interest was chosen on either the cytoplasm or the nucleus. The Pearson's R value was used for measuring colocalization of two channels.

**3D ATAC-PALM imaging. Sample preparation for 3D ATAC-PALM imaging.** We prepared samples for 3D ATAC-PALM experiments as reported previously<sup>35,44</sup>. HEK293T cells were plated onto 5-mm coverslips (Warner Instruments, cat. no. 64-0700) at around 80% confluence with fibronectin coating 1 d before the experiment. Control cells or cells treated with sorbitol for less than 5 min were fixed with 4% PFA (Electron Microscopy Sciences, cat. no. 15710) for 10 min at room temperature. After fixation, the cells were washed three times in 1×PBS for 5 min and then permeabilized in ATAC lysis buffer (10 mM Tris-Cl, pH 7.4, 10 mM NaCl, 3 mM MgCl<sub>2</sub>, and 0.1% Igepal CA-630) for 10 min at room temperature. After permeabilization, the coverslips were washed twice in 1×PBS. The transposase-mixture solution was prepared according to a previous report<sup>44</sup> and added to the cells. The sample was incubated in a humidity chamber box for 30 min at 37 °C. After incubation, the coverslips were washed three times for 15 min at 55 °C with 1×PBS containing 0.01% SDS and 50 mM EDTA before being mounted onto the lattice light-sheet microscope slot for 3D ATAC-PALM imaging.

**3D ATAC-PALM image acquisition and processing.** The 3D ATAC-PALM imaging was performed following published procedures<sup>44</sup> using lattice light-sheet microscopy<sup>37</sup>. The light sheet was generated from the interference of highly parallel beams in a square lattice and dithered to create a uniform excitation sheet. The inner and outer numerical apertures of the excitation sheet were set as 0.44 and 0.55, respectively, during experiments. To maintain stable imaging conditions at particular constant-salt concentrations, a variable-flow peristaltic pump (Thermo Fisher Scientific) was used to connect a 21 reservoir with 1×PBS circulating through the imaging chamber at a constant flow rate. The labelled cells were placed into the imaging chamber and each image volume included 100–200 image frames. Fluorescent PA-JF549 dye was initially pushed into the dark state through repeated

photobleaching by maximal laser power (2 W; MPB Communications Inc.). The samples were then imaged by iteratively photoactivating each focal plane with 405 nm light at a very weak intensity (<0.05 mW power at the rear aperture of the excitation objective and 6 W cm<sup>-2</sup> power at the sample) for 8 ms, followed by excitation of each plane with a 2 W 560 nm laser at full power (26 mW power at the rear aperture of the excitation objective and 3,466 W cm<sup>-2</sup> power at the sample) for an exposure time of 20 ms. The specimen was illuminated when the laser light went through a custom 0.65 numerical aperture (NA) excitation objective (Special Optics) and the fluorescence generated in the specimen was collected by a detection objective (CFI Apo LWD 25×W, 1.1 NA; Nikon), filtered through a 440/521/607/700 nm BrightLine quad-band bandpass filter (Semrock) and N-BK7 mounted plano-convex round cylindrical lens (f=1,000 mm, 25.4 mm diameter; Thorlabs), and eventually recorded using an ORCA-Flash 4.0 sCMOS camera (Hamamatsu).

We embedded nano-gold fiducials in the coverslips for drift correction during the imaging process as previously described<sup>38</sup>. ATAC-PALM images were taken to construct a 3D volume when the sample was moving along the sample axis. Individual volumes per acquisition were automatically stored as Tiff stacks, which were then analysed by in-house scripts written in Matlab. The cylindrical lens introduced astigmatism in the detection path and recorded each isolated single molecule with its ellipticity, thereby encoding the 3D position of each molecule relative to the focal plane of the microscope. The localization precision was estimated to be  $26 \pm 3$  nm (x and y) and  $53 \pm 5$  nm (z) by calculating the s.d. of all of the localization coordinates (x, y and z) after the nano-gold fiducial correction.

Equations used for processing raw ATAC-PALM data are in Supplementary Note 1.

**DBSCAN analysis.** The Density-based spatial clustering of applications with noise (DBSCAN) algorithm was adopted to map and visualize individual local accessible chromatin domains (core DBSCAN Matlab code from <http://yarpiz.com/255/ypml110-dbscan-clustering>). The algorithm first finds the neighbouring data points within a sphere of radius *r* and adds them into the same group. In parallel, a pre-defined threshold minimal points (*minPts*) was used by the algorithm to verify whether any counted group was a cluster. The data point was classified as noise if the number of points in a group was below the threshold *minPts*. We implemented DBSCAN analysis on the localization data for both the control cells and cells treated with sorbitol for 5 min using 150 nm as the searching radius (*r*; peak radius from the Ripley's H-function analysis) and empirically setting *minPts* as ten. The convex hull of each accessible chromatin cluster was calculated and visualized using Matlab to reconstruct the iso-surface for each identified accessible chromatin cluster. The volume of the convex hull was computed and the normalized cluster radius (calculated from a sphere with equal volume) was calculated and shown in a violin plot.

**Statistics and reproducibility.** No statistical methods were used to pre-determine the sample sizes. Some experiments were randomized and the investigators were blinded to allocation during experiments and outcome assessment. At least 20 images were taken for each experiment involving live-cell imaging or immunofluorescence and three repeats were performed for each experiment. The sample sizes were considered sufficient given that large differences, with a *P* value lower than 0.01, between the two experimental conditions were usually detected.

All of the quantitative data shown represent the mean  $\pm$  s.e.m. Bar plots have been overlaid with dot plots showing all of the individual measured data points.

No outlier suggestions were computed. No strongly scattering data points were excluded; all quantitative evaluation data points were taken into account and averaged to fully represent biological and technical variabilities.

Statistical analyses were done using the GraphPad Prism software. Statistical significance calculations comparing two conditions were performed using a two-tailed unpaired Student's *t*-test (normal data distribution), two-tailed paired Student's *t*-test or Mann-Whitney *U*-test.

The experiments were repeated at least three times and were reproducible.

**Reporting Summary.** Further information on research design is available in the Nature Research Reporting Summary linked to this article.

## Data availability

Source data for Figs. 2–8 and Extended Data Figs. 1–5 and 7 are available online. All other data supporting the findings of this study are available from the corresponding author on reasonable request.

## Code availability

The software for identifying, localizing and plotting single-molecule data is freely available after execution of a research license with HHMI. The software for the *g(r)* and DBscan analysis is freely available from [https://github.com/ammondongp/3D\\_ATAC\\_PALM](https://github.com/ammondongp/3D_ATAC_PALM).

## References

43. Ran, F. A. et al. Genome engineering using the CRISPR-Cas9 system. *Nat. Protoc.* 8, 2281–2308 (2013).

44. Chen, X. Q. et al. ATAC-seq reveals the accessible genome by transposase-mediated imaging and sequencing. *Nat. Methods* **13**, 1013–1020 (2016).

### Acknowledgements

We thank the members of the J.L.-S. lab for their helpful discussions and critical comments. Support for this work was received from the Howard Hughes Medical Institute (to J.L.-S. and Z.L.), Damon Runyon Cancer Research Foundation (grant no. DRG-2233-15 to D.C.), and intramural research funding from the NIH. We also appreciate the help we received from the Flow Cytometry Core Facility of the NEI/NIH.

### Author contributions

D.C. and J.L.-S. conceived and designed the study. D.C., D.F., P.D., E.F. and S.S. performed the experiments. D.C. and J.L.-S. wrote the manuscript

with constructive input from all authors. M.G., N.P.-S., S.S. and Z.L. provided supervision.

### Competing interest

The authors declare no competing interests.

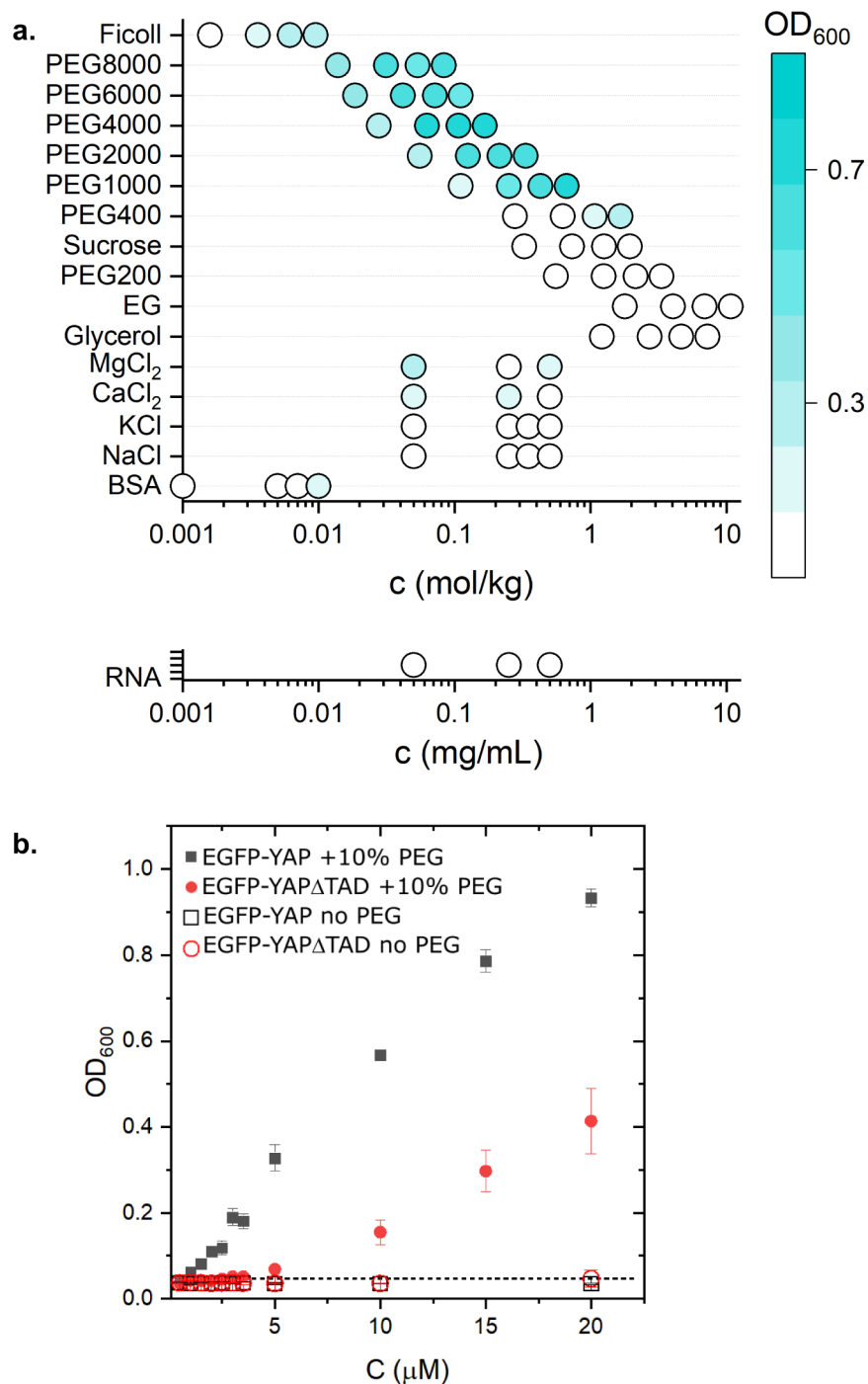
### Additional information

**Extended data** is available for this paper at <https://doi.org/10.1038/s41556-019-0433-z>.

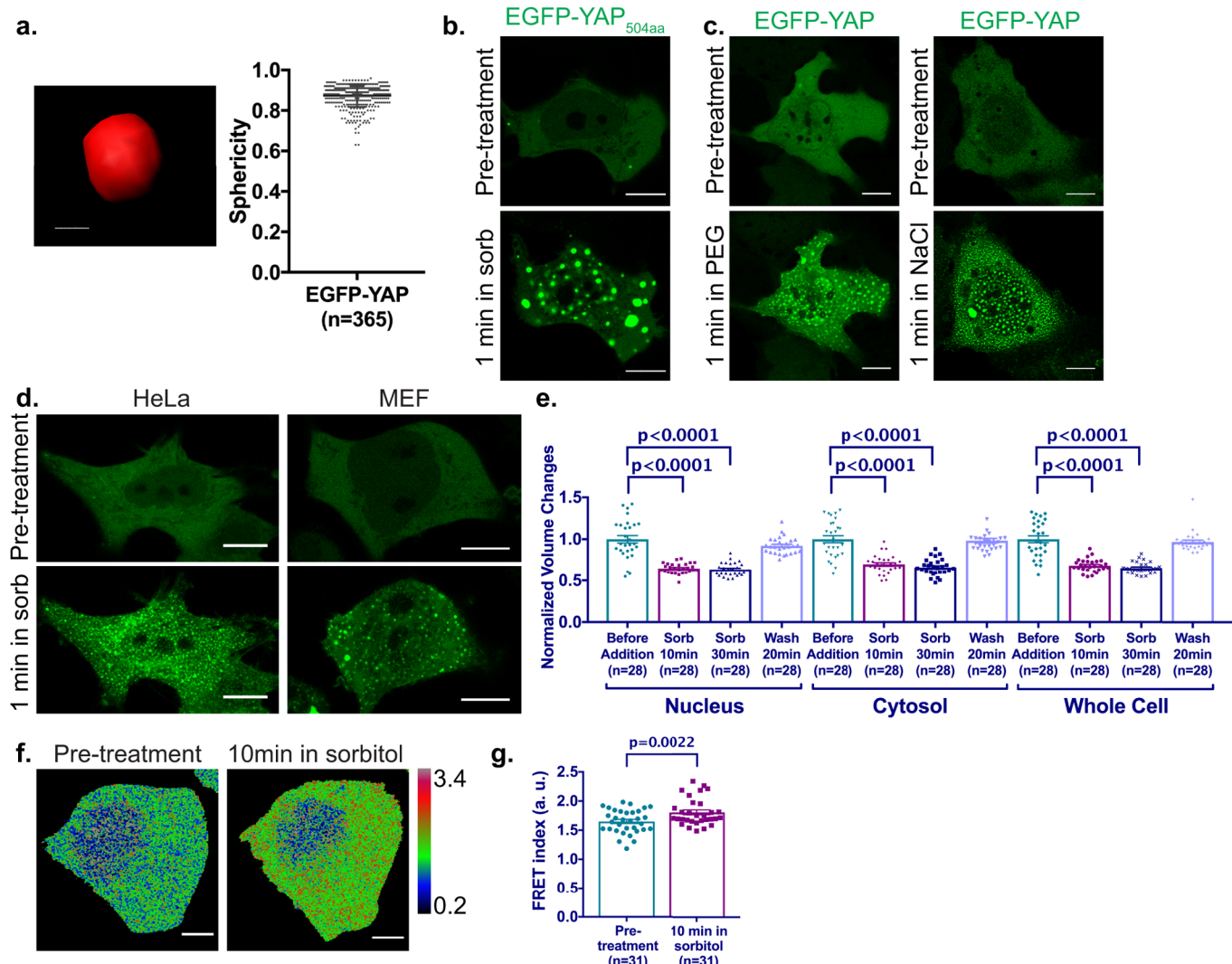
**Supplementary information** is available for this paper at <https://doi.org/10.1038/s41556-019-0433-z>.

**Correspondence and requests for materials** should be addressed to J.L.-S.

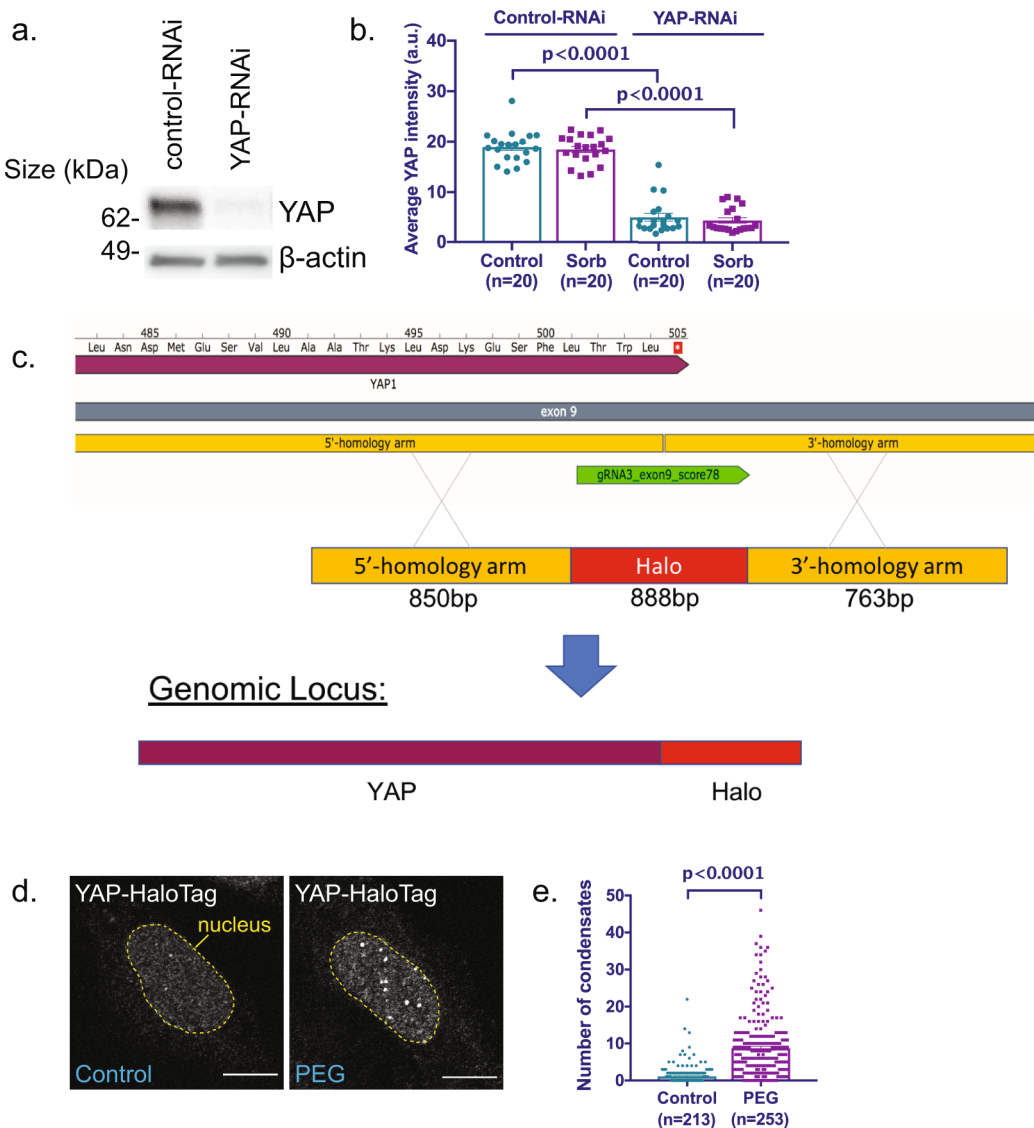
**Reprints and permissions information** is available at [www.nature.com/reprints](http://www.nature.com/reprints).



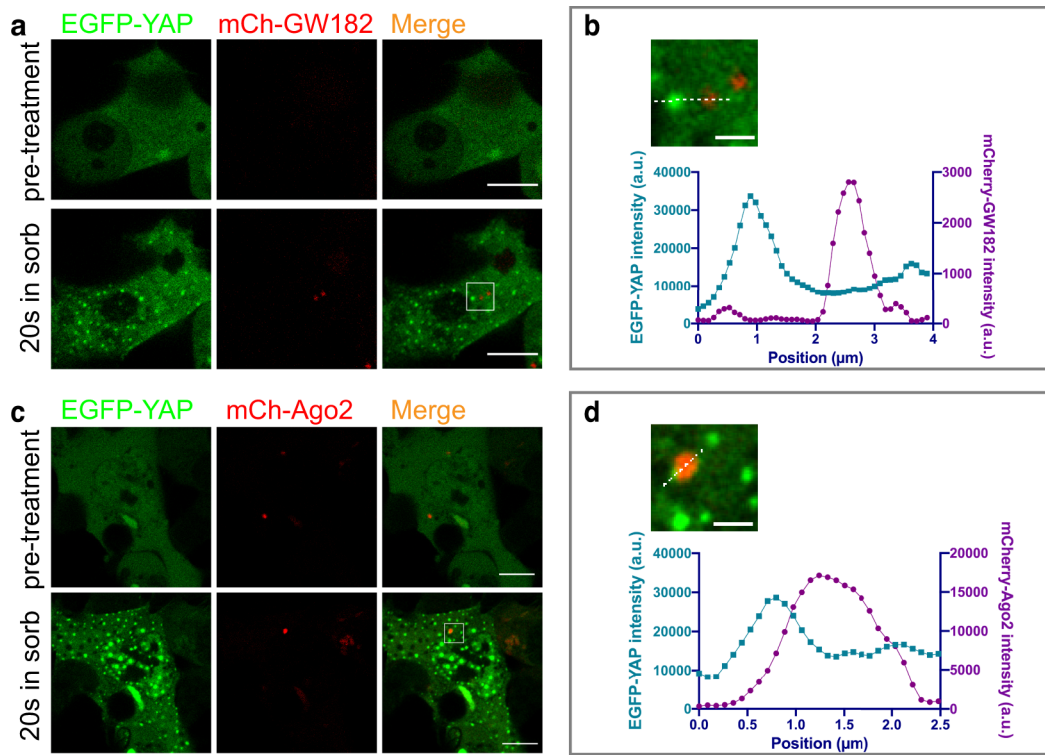
**Extended Data Fig. 1 | More characterizations of recombinant YAP protein in vitro.** **a.**, Turbidity measurements of purified EGFP-YAP at different salt, BSA and RNA concentrations. The experiment has been repeated 3 times independently with similar results. **b.**, In vitro turbidity assay showing purified EGFP-YAP phase separates at much lower concentrations than EGFP-YAP $\Delta$ TAD in the presence of 10% PEG2000. Error bars are SD from three repeats. Centre of the data is mean. n=3 biologically independent experiments. Statistics source data are provided in Source Data Extended Data Fig. 1. Source data.



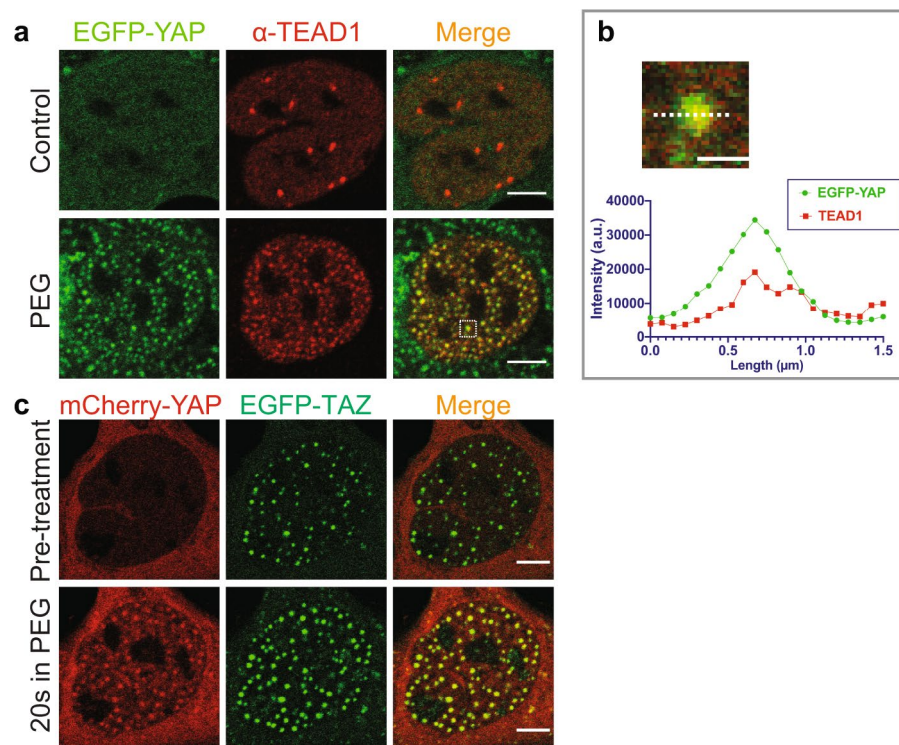
**Extended Data Fig. 2 | EGFP-YAP condensates form in hyperosmotic stress.** **a.** Imaris 3-D rendering of an EGFP-YAP condensate, and quantification of sphericity of those condensates using Imaris. Centre of the data is mean. Error bars are SD. Scale bar: 0.5μm. **(b-d)** Live-cell imaging of EGFP-YAP in HEK293T cells showing nuclear and cytoplasmic condensates are able to form with different isoforms of YAP **b**, and in different hyperosmotic agents **c**. **d**, Live-cell imaging showing different cell types are able to form EGFP-YAP condensates under hyperosmotic stress. Scale bars are 10μm. All the experiments are repeated 3 times independently with similar results. **e**, Quantification of normalized HEK293T nuclear, cytosolic and total volume before and after sorbitol treatment, and after wash. Centre of the data is mean. Error bars are s.e.m. Two-sided paired t-test. Comparing to volume before treatment. Error bars show s.e.m. n=28 biologically independent samples. **(f, g)** Representative ratiometric images **f**, and quantification **g**, of crowding sensor FRET expressed in the same HEK293T cell before and after 0.2M sorbitol treatment. Rainbow RGB look-up table showing changes in FRET indices. Colour bar: FRET index (a.u.). Two-sided paired t-test. Centre of the data is mean. Error bars show s.e.m. Scale bars are 5μm. n=31 biologically independent samples. Statistics source data are provided in Source Data Extended Data Fig. 2.



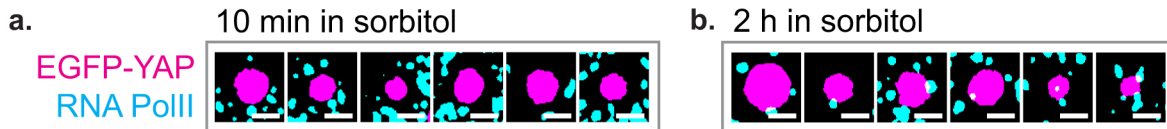
**Extended Data Fig. 3 | Endogenous YAP forms condensates.** **(a, b)** Immunoblotting experiments **a**, and quantifications of immunofluorescence YAP signal **b**, indicate that YAP signal is effectively knocked down by YAP siRNA. Two-sided unpaired *t*-test is used in **b**. Centre of the data is mean. Error bars show s.e.m. All the experiments are repeated 2 times independently with similar results.  $n=20$  biologically independent samples. **c**, Schematics of construction of CRISPR knock-in YAP-HaloTag U-2 OS cell line. Live-cell imaging **d**, and quantification **e**, showing nuclear YAP-HaloTag condensate labelled by JF549 Halo dye increases in number after PEG 300 treatment. Two-sided unpaired *t*-test analysis. Centre of the data is mean. Error bars show s.e.m. Scale bars are 10 $\mu$ m.  $n=213$  biologically independent control samples.  $n=253$  biologically independent PEG-treated samples. Statistics source data are provided in Source Data Extended Data Fig. 3. Unprocessed blots are provided in Unprocessed Blots Extended Data Fig. 3.



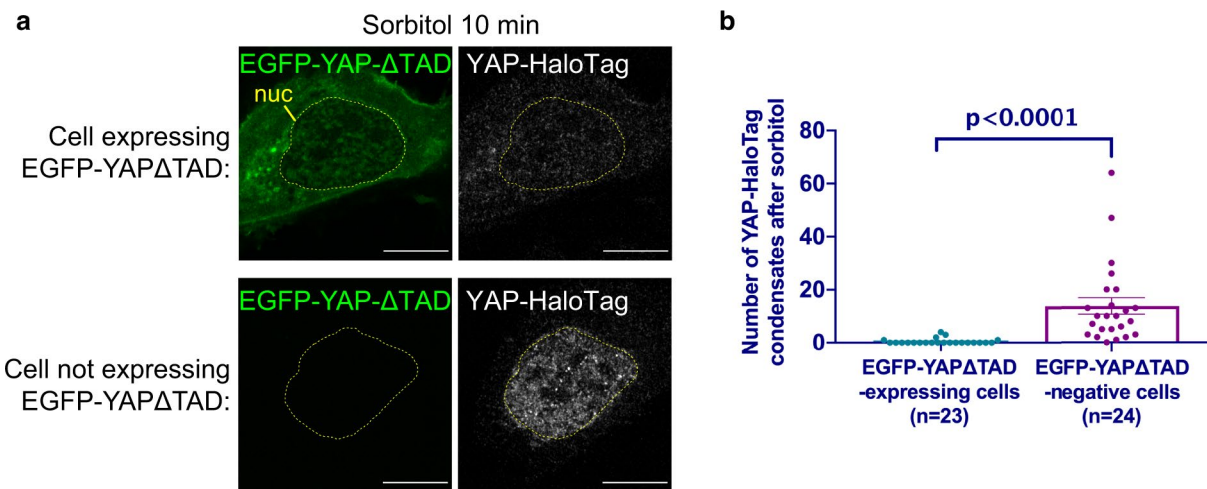
**Extended Data Fig. 4 | Characterization of cytoplasmic YAP condensates.** **a**, Live-cell imaging showing no colocalization of cytoplasmic EGFP-YAP condensates with P-body component mCherry-GW182 after 0.2 M sorbitol treatment for 20 s in HEK293T cells. **b**, Magnification of boxed region in (a) and line scan. **(c, d)** Similar to (a, b), showing no colocalization of EGFP-YAP cytoplasmic condensates with mCherry-Ago2 after 0.2 M sorbitol treatment for 20 s. Scale bars are 10 μm in whole-cell view, and are 2 μm in magnified view. All the experiments are repeated 3 times independently with similar results. Numerical source data are provided in Source Data Extended Data Fig. 4.



**Extended Data Fig. 5 | Characterization of nuclear YAP condensates.** **a**, Representative immunofluorescence images showing EGFP-YAP nuclear condensates colocalize with endogenous TEAD1 under hyperosmotic stress in U-2 OS cells. **b**, Magnification of boxed region in a, and line scan. Scale bar: 1 $\mu\text{m}$ . **c**, Live-cell imaging showing mCherry-YAP localizes to EGFP-TAZ condensates and new condensates after hyperosmotic stress in U-2 OS cells. Scale bars in (a) and (c) are 5 $\mu\text{m}$ . All the experiments are repeated 3 times independently with similar results. Numerical source data are provided in Source Data Extended Data Fig. 5.



**Extended Data Fig. 6 | Dynamic localization of RNAPII relative to EGFP-YAP nuclear condensates after hyperosmotic shock.** **a**, More examples showing no colocalization of RNAPII (pSer2) with EGFP-YAP condensates at 10min in 0.2M sorbitol. Experiments are same as those in Fig. 7b, EGFP-YAP condensates are auto-thresholded and turned into mask using ImageJ, and pseudo-coloured magenta. RNAPII immunofluorescence is autothresholded and turned into mask using ImageJ, and pseudo-coloured cyan. **b**, Similar to a, but showing more examples of enhanced localization of RNA Pol II (pSer2) to the periphery of EGFP-YAP condensates at 2 h in sorbitol. All the experiments are repeated 3 times independently with similar results. Scale bars are 1 $\mu$ m.



**Extended Data Fig. 7 | EGFP-YAP $\Delta$ TAD mutant serves as a dominant negative protein that decreases endogenous YAP foci.** **a**, Immunofluorescence images of YAP-HaloTag U-2 OS cells 10 min in sorbitol treatment, with EGFP-YAP $\Delta$ TAD overexpression (top row) or without (bottom row). Scale bars are 10 $\mu$ m. **b**, Quantification showing YAP-HaloTag U-2 OS cells have lower number of YAP-HaloTag endogenous YAP condensates after sorbitol treatment for 10 min, if they overexpress EGFP-YAP $\Delta$ TAD construct. Two-sided unpaired *t*-test. Centre of the data is mean. Error bars show s.e.m. *n*=23 biologically independent EGFP-YAP $\Delta$ TAD-expressing samples. *n*=24 biologically independent EGFP-YAP $\Delta$ TAD-negative samples. Statistics source data are provided in Source Data Extended Data Fig. 8.

## Reporting Summary

Nature Research wishes to improve the reproducibility of the work that we publish. This form provides structure for consistency and transparency in reporting. For further information on Nature Research policies, see [Authors & Referees](#) and the [Editorial Policy Checklist](#).

### Statistics

For all statistical analyses, confirm that the following items are present in the figure legend, table legend, main text, or Methods section.

n/a Confirmed

- The exact sample size ( $n$ ) for each experimental group/condition, given as a discrete number and unit of measurement
- A statement on whether measurements were taken from distinct samples or whether the same sample was measured repeatedly
- The statistical test(s) used AND whether they are one- or two-sided  
*Only common tests should be described solely by name; describe more complex techniques in the Methods section.*
- A description of all covariates tested
- A description of any assumptions or corrections, such as tests of normality and adjustment for multiple comparisons
- A full description of the statistical parameters including central tendency (e.g. means) or other basic estimates (e.g. regression coefficient) AND variation (e.g. standard deviation) or associated estimates of uncertainty (e.g. confidence intervals)
- For null hypothesis testing, the test statistic (e.g.  $F$ ,  $t$ ,  $r$ ) with confidence intervals, effect sizes, degrees of freedom and  $P$  value noted  
*Give P values as exact values whenever suitable.*
- For Bayesian analysis, information on the choice of priors and Markov chain Monte Carlo settings
- For hierarchical and complex designs, identification of the appropriate level for tests and full reporting of outcomes
- Estimates of effect sizes (e.g. Cohen's  $d$ , Pearson's  $r$ ), indicating how they were calculated

*Our web collection on [statistics for biologists](#) contains articles on many of the points above.*

### Software and code

Policy information about [availability of computer code](#)

Data collection

We used Zen software from Zeiss to collect confocal and airyscan images in this study.

Data analysis

We used Imaris (Bitplane) to reconstruct three-dimensional images, ImageJ to perform colocalization analysis (Coloc 2) and image visualization. We used GraphPad Prism to perform statistical analysis. For ATAC-PALM data, software for identifying, localizing and plotting single-molecule data is freely available after execution of a research license with HHMI. The software for G(r) and DBscan analysis is freely available from [https://github.com/ammondongp/3D\\_ATAC\\_PALM](https://github.com/ammondongp/3D_ATAC_PALM)

For manuscripts utilizing custom algorithms or software that are central to the research but not yet described in published literature, software must be made available to editors/reviewers. We strongly encourage code deposition in a community repository (e.g. GitHub). See the Nature Research [guidelines for submitting code & software](#) for further information.

### Data

Policy information about [availability of data](#)

All manuscripts must include a [data availability statement](#). This statement should provide the following information, where applicable:

- Accession codes, unique identifiers, or web links for publicly available datasets
- A list of figures that have associated raw data
- A description of any restrictions on data availability

Source data for Figs. 2-8 and Supplementary Figs. 1-5 and 8 have been provided as Supplementary Table. All other data supporting the findings of this study are available from the corresponding author on reasonable request.

# Field-specific reporting

Please select the one below that is the best fit for your research. If you are not sure, read the appropriate sections before making your selection.

Life sciences       Behavioural & social sciences       Ecological, evolutionary & environmental sciences

For a reference copy of the document with all sections, see [nature.com/documents/nr-reporting-summary-flat.pdf](http://nature.com/documents/nr-reporting-summary-flat.pdf)

## Life sciences study design

All studies must disclose on these points even when the disclosure is negative.

Sample size	At least 20 images are taken for each experiment, and 3 repeats are performed for each experiment. The sample size is sufficient since we usually detect large difference between two experimental conditions, with p-value lower than 0.01.
Data exclusions	No data is excluded from this study.
Replication	All attempts at replication are successful.
Randomization	Not relevant to the study.
Blinding	The investigator is blinded to the sample at data collection.

## Reporting for specific materials, systems and methods

We require information from authors about some types of materials, experimental systems and methods used in many studies. Here, indicate whether each material, system or method listed is relevant to your study. If you are not sure if a list item applies to your research, read the appropriate section before selecting a response.

Materials & experimental systems		Methods	
n/a	Involved in the study	n/a	Involved in the study
<input type="checkbox"/>	<input checked="" type="checkbox"/> Antibodies	<input checked="" type="checkbox"/>	<input type="checkbox"/> ChIP-seq
<input type="checkbox"/>	<input checked="" type="checkbox"/> Eukaryotic cell lines	<input checked="" type="checkbox"/>	<input type="checkbox"/> Flow cytometry
<input checked="" type="checkbox"/>	<input type="checkbox"/> Palaeontology	<input checked="" type="checkbox"/>	<input type="checkbox"/> MRI-based neuroimaging
<input type="checkbox"/>	<input checked="" type="checkbox"/> Animals and other organisms		
<input checked="" type="checkbox"/>	<input type="checkbox"/> Human research participants		
<input checked="" type="checkbox"/>	<input type="checkbox"/> Clinical data		

## Antibodies

Antibodies used	anti-YAP (Cell Signaling 14074S, Lot 4, 1:150); anti-TEAD1 (BD Biosciences 610922, Lot 6228876, 1:200); anti-RNA polymerase II CTD repeat YSPTSPS (phospho S2) (Abcam ab193468, 1:150); anti-G3BP1 (proteintech 13057-2-AP, 1:5000); anti-PML (Abcam ab96051, Lot GR3174201-1, 1:500); and anti-Coilin (Abcam ab87913, Lot GR50257-4, 1:200)
Validation	All primary antibodies are validated on the manufacturer's website. Anti-YAP is validated by RNAi knockdown.

## Eukaryotic cell lines

Policy information about <a href="#">cell lines</a>	
Cell line source(s)	U2-OS (gift from Lingfeng Chen) and HEK293T (gift from Anirban Banerjee Lab)
Authentication	None of the cell lines are authenticated.
Mycoplasma contamination	Mycoplasma contamination is tested with MycoAlert™ Mycoplasma Detection Kit-Lonza.
Commonly misidentified lines (See <a href="#">ICLAC</a> register)	No ICLAC cell lines have been used in this study.

## Animals and other organisms

Policy information about [studies involving animals](#); [ARRIVE guidelines](#) recommended for reporting animal research

Laboratory animals

Eight-weeks female (FVB/NJ) mice were purchased from The Jackson Laboratory (<https://www.jax.org>).

Wild animals

*Provide details on animals observed in or captured in the field; report species, sex and age where possible. Describe how animals were caught and transported and what happened to captive animals after the study (if killed, explain why and describe method; if released, say where and when) OR state that the study did not involve wild animals.*

Field-collected samples

*For laboratory work with field-collected samples, describe all relevant parameters such as housing, maintenance, temperature, photoperiod and end-of-experiment protocol OR state that the study did not involve samples collected from the field.*

Ethics oversight

All procedures were performed according to protocols (LCMB-037) approved by the veterinary authorities at NIH/NCI.

Note that full information on the approval of the study protocol must also be provided in the manuscript.